TRIBOLOGICAL AND CAVITATION EROSION BEHAVIOR OF METALLIC GLASS REINFORCED ALUMINUM MATRIX COMPOSITES PROCESSED USING SPARK PLASMA SINTERING

By

SHUBHANKAR PADWAL

Bachelor of Technology in Metallurgical Engineering

May, 2018

College of Engineering Pune

Maharashtra, India

Submitted to the Faculty of the
Graduate College of the
Oklahoma State University
in partial fulfillment of
the requirements for
the Degree of
MASTER OF SCIENCE
July, 2020

TRIBOLOGICAL AND CAVITATION EROSION BEHAVIOR OF METALLIC GLASS REINFORCED ALUMINUM MATRIX COMPOSITES PROCESSED USING SPARK PLASMA SINTERING

Thesis Approved:

Dr. Sandip P. Harimkar

Thesis Adviser

Dr. A. Kaan Kalkan

Dr. Ritesh Sachan

ACKNOWLEDGMENTS

This material is based upon work supported by the National Science Foundation (NSF) under Grant No. CMMI-1462602.

I want to express my deep and sincere gratitude to my advisor Dr. Sandip P. Harimkar, for allowing me to join his research group and guiding me to do good research. When you have an advisor who nurtures your ideas and encourages you to strive for the best, research becomes interesting. His passion for research always kept me motivated. Without his support, trust, and guidance, it would not have been possible to complete the research successfully. I am grateful to him. I would like to extend my heartfelt thanks to him and his family.

I earnestly convey my thanks to Dr. A. Kaan Kalkan and Dr. Ritesh Sachan for accepting to be my thesis committee member instantly with all kindness when I approached.

I would like to thank my parents, Mr. Santosh Padwal and Ms. Komal Padwal, whose love and guidance are with me in whatever I pursue. I am because they are. I wish to thank my senior Dr. Tanaji Paul, who played an extremely crucial role as a mentor friend. I would like to acknowledge my colleagues and friends for their help, support, and adding some spice to my otherwise monotonous life.

Acknowledgements reflect the views of the author and are not endorsed by committee members or Oklahoma State University.

Name: SHUBHANKAR PADWAL

Date of Degree: JULY, 2020

Title of Study: TRIBOLOGICAL AND CAVITATION EROSION BEHAVIOR OF METALLIC GLASS REINFORCED ALUMINUM MATRIX COMPOSITES PROCESSED USING SPARK PLASMA SINTERING

Major Field: MECHANICAL AND AEROSPACE ENGINEERING

Abstract: Metallic glasses are emerging as a potential reinforcement for lightweight metal matrix composites. With their high strength, high elastic strain limit, and metallic nature, metallic glasses have better prospects of improving the mechanical performance of the composites, providing a viable alternative to conventional ceramic reinforcements. With improved matrix-reinforcement interfacial characteristics, metallic glass reinforced composites can exhibit excellent sliding wear and cavitation erosion resistance. In the present research, we report on spark plasma sintering (SPS) and wear characterization of novel lightweight Al-based composites reinforced with varying volume content of Fe-based metallic glass (FMG) of composition $Fe_{48}Cr_{15}Mo_{14}Y_2C_{15}B_6$. SPS processing in the supercooled liquid region (between T_{x1} and T_g) prevents the devitrification of metallic glass and assists the densification. In the first objective, dry sliding wear resistance of the composites is investigated using a tribometer. A significant improvement in wear resistance is reported with the addition of the FMG reinforcement. Wear behavior of the composites is studied by analyzing the worn surfaces with profilometry, SEM, and EDS. Outcomes of this research offer insights into the wear behavior of metallic glass reinforced metal matrix composites. In the second objective, the cavitation erosion behavior of the composites using a vibratory cavitation tester is investigated. The results show that the composites have superior resistance to the surface deformation than pure aluminum, and the resistance to deformation increases with an increase in the reinforcement content. Surface profiles of the exposed region are analyzed to quantify the penetration depth distribution, and it is observed that the presence of reinforcement particles mitigates the distortion caused by micro-jets. SEM reveals the morphology of the affected area, indicating that localized matrix material removal is caused by ductile tearing, followed by brittle fracture across the interface and detachment of the reinforcement particle from the surface. The results are further explained based on the influence of reinforcement particle contiguity on the cavitation erosion.

TABLE OF CONTENTS

Chapter		Page
I. METAL MATRIX COMPOSITES …….		1
1.1	Importance of metal matrix composites (MMCs) ……	1
1.2	Characteristics of MMCs ……..	2
1.2.1	Matrix nature ……	2
1.2.2	Reinforcement nature ……...	3
1.2.3	Reinforcement-matrix interface ……...	5
1.3	Importance of interfacial bonding ……	5
1.4	Metallic glass as a reinforcement …….	7
II. REVIEW OF METALLIC GLASS REINFORCED ALUMINUM MATRIX COMPOSITES ……		10
2.1	Ni-based metallic glass reinforced composites ……...	10
2.2	Ti-based metallic glass reinforced composites …….	11
2.3	Cu-based metallic glass reinforced composites ……	15
2.4	Zr-based metallic glass reinforced composites …….	15
2.5	Processing of composites using spark plasma sintering ……...	16
2.6	Sliding wear ……..	19
2.7	Cavitation erosion …….	20
III. OBJECTIVES AND EXPERIMENTAL METHODOLOGY ……..		24
3.1	Objectives	24
3.1.1	Objective 1: Dry sliding wear behavior of Al-FMG composites..	24
3.1.2	Objective 2: Cavitation erosion behavior of Al-FMG composites..	24
3.2	Experimental methodology ……..	25
IV. RESULTS AND DISCUSSION …….....		27
4.1	Dry sliding wear behavior of the composite ……	27
4.1.1	Microstructure and phase analysis ……...	27
4.1.2	Consolidation and mechanical strength prediction ……..	30
4.1.3	Wear analysis ……...	33

Chapter Page

4.2 Cavitation erosion behavior of the composite …… 40
4.2.1 Microstructure ……. 40
4.2.2 Cavitation erosion behavior …… 42
4.2.3 Erosion mechanism ……. 46

V. CONCLUSIONS …….. 51

5.1 Dry sliding wear behavior of the composites ……. 51
5.2 Cavitation erosion behavior of the composites ……... 52

REFERENCES …….. 53

LIST OF TABLES

Table		Page
1.1	Commonly used ceramic reinforcements with the average particle size [10] ……..	3
1.2	Effect of micro-sized and nano-sized SiC reinforcements on the tensile strength and elongation limit of A356 alloy [11-12] ……...	4
4.1	Reinforcement weight fractions, Vickers's micro-hardness values, and volume wear rates of composites ……	30

LIST OF FIGURES

Figure		Page
1.1	Wetting angle and surface energies at the phase interface ……...	6
2.1	XRD patterns of the sintered Al7075 alloy without the reinforcement and the composite [34] ……..	12
2.2	Compressive stress-strain curve of the composite compared with unreinforced Al7075 (a) and SEM micrographs of the fracture surface of the composite after failure (b and c) [34] ……	12
2.3	Variation in the relative density and density as a function of reinforcement content [37] …….	14
2.4	Compressive stress-strain curves the matrix material and composites reinforced with varying content of Ti-based metallic glass [37] …….	14
2.5	(a) Schematic of spark plasma sintering process [40], (b) Current flow through powder particles [41] …….	17
2.6	Bright-field TEM and SAED imaging of Al7075-metallic glass composite [47] ……..	18
2.7	IFFT-TEM imaging of the interfacial area highlighting the stacking faults [47] ……..	18
2.8	Phase diagram of water [53] ……	21
2.9	Schematic of cavitation erosion testing setup …….	21
4.1	Optical micrographs of consolidated composites (a) Al-10 FMG, (b) Al-20 FMG, (c) Al-30 FMG, (d) Al-40 FMG, and (e) Al-50 FMG ……...	28
4.2	XRD patterns of $Fe_{48}Cr_{15}Mo_{14}Y_2C_{15}B_6$/Al composites fabricated by spark plasma sintering ……..	29

Figure Page

4.3 SEM micrograph and elemental composition plot of the interfacial region in Al-30 FMG composite …….. 30

4.4 Calculated and experimental density as a function of FMG reinforcement content ……. 31

4.5 Hardness and the calculated ratio of yield strength of composite to matrix as a function of FMG reinforcement content ……. 33

4.6 Wear depth profiles of (a) pure Al (b)Al-10 FMG, (c)Al-20 FMG, (d) Al-30 FMG, (e) Al-40 FMG, and (f) Al-50 FMG composites ……. 34

4.7 Volume loss and degree of wear as a function of FMG reinforcement content ……... 36

4.8 SEM images of the wear profiles of (a) pure Al (b) Al-10 FMG (c) Al-20 FMG (d) Al-30 FMG (e) Al-40 FMG, and (f) Al-50 FMG …… 37

4.9 EDS elemental maps from the worn surfaces of (a) Al-10 FMG (b) Al-30 FMG, and (c) Al-50 FMG ……. 38

4.10 Back scattered electron micrographs of the consolidated composites (a) Al-10 FMG, (b) Al-20 FMG, (c) Al-30 FMG, and (d) Al-40 FMG …… 40

4.11 Elemental composition on the reinforcement, the interface, and the matrix region ……. 41

4.12 Worn out areas of all the composites scanned with the profilometer …….. 42

4.13 (a) The average depth of penetration as a function of exposure time. (b) Measured volume loss of the specimens vs FMG reinforcement content 44

4.14 Splitting the wear profile of Al-20 FMG into clusters …… 45

4.15 Area occupancy of several depth clusters after exposing the specimens for (a) 5 min, (b) 15 min, and (c) 25 min …… 45

4.16 SEM micrographs of (a) pure Al, and the composites (b) Al-10FMG, (c) Al-20 FMG, (d) Al-30 FMG, and (e) Al-40 FMG after being exposed to the cavitation for 15 min …… 47

4.17 Backscattered Electron image of cavitation eroded Al-10 FMG composite …….. 48

4.18 Cavitation erosion stages explained using the schematic ……... 49

4.19 Elemental mapping of Al-30 FMG after being exposed to the cavitation 50

CHAPTER I

METAL MATRIX COMPOSITES

1.1 Importance of metal matrix composites

At present, rising concerns over the global energy crisis have accelerated the research in materials development. Metal matrix composites (MMCs) are claimed to be a viable solution to the increasing demand for lightweight, fuel-efficient, and environmentally friendly material. Over the years, MMCs have emerged as an essential class of structural material. With persistent research in the past, now metal-based composites are making a significant contribution to engineering practices. The improvement in the MMCs is the consequence of development in the processing techniques and advancements in the understanding of the structure-property relationship at the greater depth through cutting edge state-of-the-art research instruments. Ductility and toughness of metals combined with high strength and modulus of second phase reinforcement enable the usage of composites in rigorous conditions such as high temperature and high friction. With advancements in manufacturing methods, MMCs have already started replacing conventional metallic parts in weight imperative applications such as automobile and aerospace [1-2].

Excellent thermomechanical properties paired with superior corrosion resistance make AMCs an ideal structural material. Morphology of the reinforcement (particle, whisker, fiber) and nature of the interface play a pivotal role in determining the final properties of the composite. In the pursuit of achieving high performance and efficiency through weight reduction, research is being focused on developing lightweight metal matrix composites. Aluminum matrix composites (AMCs) possess remarkable mechanical properties such as high strength-to-weight ratio and high toughness. The commercially used reinforcement phases are oxides (Al_2O_3), carbides (SiC, B_4C), nitrides (AlN, Si_3N_4) [3], carbon nanotubes, and graphene [4-5]. High hardness, elastic modulus, and superior refractory properties of the reinforcement phases open up a plethora of applications for AMCs in the automotive, aerospace, and military industries. However, the mechanical properties of the metal matrix composites depend primarily on the nature of the interface. In the case of ceramic reinforcement, the nature of the bonding is different at the interface as it changes from metallic in the matrix to the covalent/ ionic in the reinforcement phase [6-8]. Apart from the matrix and reinforcement material characteristics, the interaction between the matrix and the reinforcement has a remarkable effect on the microstructure, mechanical properties, and performance of the composite.

1.2 Characteristics of the metal matrix composite

1.2.1 Matrix nature

Matrix is the continuous and homogeneous phase of the composite and occupies the majority of the composite volume (>50%). Properties of the materials can be improved by introducing a suitable reinforcement in the matrix. In addition to holding the reinforcement phase at a place, the primary function of the matrix is to transfer the load efficiently. For the majority of the engineering applications, an essential requirement for a matrix material is that its fracture strain must be higher than the reinforcement. The chemical reaction resulting from high processing and working temperature alters the matrix microstructure and influences the mechanical properties of the composite. For example, the coefficient of thermal (CTE) mismatch at the matrix/reinforcement

contact induces residual stress at the interface. In the event where the interlayer formed is incompatible with the matrix, it can lead to: i) plastic deformation of the ductile matrix by grain boundary sliding, twinning, slip movement, ii) fracture of a brittle matrix phase, and iii) failure at the interface [9].

1.2.2. Reinforcement nature

Reinforcement is dispersed in the composite as a second phase. Due to the high strength and elastic modulus of the reinforcement, the load is transferred from the matrix to the reinforcement. According to the principle of combined action, the final properties of the composite depend on the individual properties of the matrix and the reinforcement and the geometry of the dispersed reinforcement phase. In conventional practice, metals are reinforced with ceramics in the discontinuous (particulate and short fibers) form or continuous fiber form. Continuous fibers are generally 100 μm or longer. As a result of their defined orientation, continuous fiber-reinforced composites exhibit anisotropic behavior. Particles, whiskers and short fibers are categorized into the discontinuous reinforcements. Some of the commercially used particle reinforcements are tabulated along with the mean particle size in **Table 1.1** [10].

Table 1.1: *Commonly used ceramic reinforcements with the average particle size* [10]

Material	Mean Size Used (μm)	Density (g/cm^3)
SiC	15 - 340	3.2
SiO_2	40 - 60	2.3
Al_2O_3	40 - 340	4.0
B_4C	40 - 300	2.5
Graphite	40 - 250	1.6-2.2
Si_3N_4	40 - 60	3.2
TiC	40 - 50	2.25

Large reinforcements have a higher statistical probability of having intrinsic defects, which can cause their early failure and reduce effectiveness. In recent studies, nano-sized reinforcements have been used, and they exhibit superior properties than their micro-sized counterparts. Some of the examples are listed in **Table 1.2** [11-12].

***Table 1.2**: Effect of micro-sized and nano-sized SiC reinforcements on the tensile strength and elongation limit of A356 alloy. CC = compo-casting* [11]

Material	Yield Strength (MPa)	Ultimate Tensile Strength (MPa)	% ductility
Micro-sized reinforcement			
A356 (T6)	205	280	6
10% SiC_p	287	308	0.5
15% SiC_p	329	336	0.2
20% SiC_p	336	357	0.4
Nano-sized reinforcement			
A356 (CC)	130	157	8
0.5 % nSiC	138	243	5.6
1.5 % nSiC	143	253	5.0
2.5 % nSiC	147	273	4.5
3.5 % nSiC	149	295	4.3
4.5 % nSiC	151	303	4.1

When the reinforcement hinders the dislocation movement, dislocation pile-ups and stacking faults are generated. The stress induced by them is calculated by Orowan's equation given by [13]:

$$\sigma = \varphi \frac{Gb}{L} \tag{1.1}$$

where L is the inter-particulate distance. Nano-particles have higher surface area than the micro-sized particles, and hence the separation distance L is shorter, leading to higher Orowan stress. This confirms that the nature of the reinforcement actively governs the mechanical properties of the composite.

1.2.3. Reinforcement-matrix interface

According to Metcalfe [14], the interface is a surface formed by a common boundary between the two constituent phases. The interface plays a crucial role in determining the final physical and mechanical properties of the composite. It occupies a particular area and facilitates the transfer of load from the matrix to reinforcement. The coefficient of thermal expansion (CTE), hardness, and elastic modulus (E) of the interface is different than the matrix and reinforcement, and the interface nature depends on the nature of the reaction between two phases. The interlayer is formed as a result of short-range atomic diffusion and acts as a nucleation site for intermetallic phases.

1.3 Importance of the interfacial bonding

An adherent and coherent interlayer allows efficient load transfer from matrix to the reinforcement and prolongs the composite life. The significant factors affecting the interfacial bond are wettability, mechanical/ chemical bonding, and thermal stress.

(a) Wettability: The ability of a phase to spread and uniformly occupy the surface of another phase is defined as wettability [9]. The interface between the involving phases is stabilized by balancing the surface energies at the contact boundary. In the composites, wettability is understood as the energy required for a metal matrix to engulf the reinforcement phase without leaving any

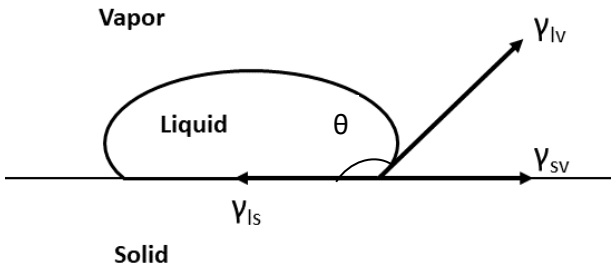

Figure 1.1*: Wetting of two phases depends on the surface tension values at the contact area.*

interfacial porosity. Fig. 1.1 indicates the surface energies at the phase boundaries $\gamma_{ls}, \gamma_{lv}, and\ \gamma_{sv}$ and the wetting angle θ. The wetting angle of 180° indicates non-wetting while 0° denotes perfect wetting. In most of the metal-ceramic pairs, the wetting angle is large, and wettability is poor. Efforts have been made to improve the wettability by coating the reinforcement and employing alloy modification techniques [15-16]. Ni is one of the well-studied coating metals that facilitates the wetting of Al with SiC and Al_2O_3 [17].

(b) Mechanical bonding and chemical reactions: Surface roughness and morphology of the reinforcement produce mechanical keying effect on the surrounding matrix phase. Rough edges and notches offer mechanical locking with the matrix and resist the particle pullout. One of the examples is documented by Metcalfe [14], where the tungsten wires were roughened before adding in aluminum. Ozsoy [18] calculated the increased stress levels caused by the reinforcement particle morphology. As discussed prior, high processing and working temperature favor the atomic movement across the boundary, eventually forming an interlayer. Properties of the interlayer depend on the bond nature of the reinforcement and the matrix, and its thickness. In most of the MMCs, nucleation of intermetallic phases, carbides or oxides at the interface deteriorates the mechanical properties of the composite. Nucleation of aluminum carbide (Al_4C_3) in Al-SiC composite is well-known for its deleterious effects on the composite. Nature of the chemical bond and mechanical bonding largely influence the properties of the composite.

(c) Thermal stress: Thermal stress is another dominant factor that affects the characteristics of the interfacial bonding. The difference in the linear coefficient of thermal expansion (CTE) between the matrix and reinforcement causes thermal mismatch, creating highly stressed zones at the interface. If the induced stress exceeds the yield stress of the matrix, the matrix undergoes local plastic deformation. This thermal stress is calculated by the following equation[19-20]:

$$\Delta\sigma_{the} = \mu\eta^{m}b^{m}\sqrt{\rho} \tag{1.2}$$

where η is a constant and ρ is the dislocation density. ρ is directly proportional to the difference in the CTE of matrix and the reinforcement, and inversely proportional to $(1-f)$, where f is the reinforcement volume fraction. The magnitude of the thermal stress influences the mechanical properties of the matrix. Dislocation density, stacking fault density, and residual stress are notably higher near the reinforcement phase. The energy stored in the stressed region also accelerates the aging in precipitation hardenable Al and Mg matrix [21]. In the research conducted by Bounafia *et al.* [22], the Al-SiC system was studied with finite element methods. Interfacial residual stress was computed to be as high as 100 MPa in the tensile direction. It was concluded that to maximize the mechanical properties of the composite, residual stress should be minimized.

1.4 Metallic glass as a reinforcement

Over the years, bulk metallic glasses (BMGs) have emerged as promising materials for structural applications owing to their high mechanical strength, high hardness, and excellent corrosion resistance. Due to the random disordered arrangement of atoms, bulk amorphous materials have neither a uniform crystal structure nor grain boundaries, unlike conventional metals and alloys. This fact primarily contributes to their high strength and superior corrosion resistance. In metals, the high energy of the system in the liquid phase is reduced by the formation of thermodynamically stable ordered crystals. Most of the metals solidify in inhomogeneous fashion. It leads to a polycrystalline microstructure with grain boundaries separating each set of the ordered lattice.

Grain boundaries are weaker areas of irregular atomic packing, where fracture and corrosion initiates. Metallic glass formation bypasses the crystallization with very high undercooling, leading to the formation of a frozen, vitreous solid solution. However, the absence of defined slip planes makes the metallic glass brittle. Practically, a very high cooling rate is required to suppress crystallization entirely.

First metallic glass produced in 1960 ($Au_{80}Si_{20}$) employed the cooling rate of 1×10^6 °C s^{-1} [23]. The presence of rare earth elements, aluminum, boron in the composition enhances the Glass Forming Ability (GFA) and delay the devitrification of the alloy. Some of the Fe-based metallic glasses, such as $Fe_{52.5}Cr_{7.5}Mo_{15}C_{15}B_{10}$, $Fe_{45}Cr_{15}Mo_{15}C_{15}B_{10}$, and $(Fe_{0.75}B_{0.15}Si_{0.10})_{99}Zr_1$ are reported to have a broad supercooled liquid region (SCLR), and hence, good GFA [24]. $(Zr_{82.5}Ti_{17.5})_{55}(Ni_{54}Cu_{46})_{18.75}Be_{26.25}$ has one of the widest reported super-cooled regions of 135 K [31-32]. High SCLR also assists densification in powder processing of the metallic glass. With impressive physical and mechanical properties, metallic glass is emerging as the potential candidate for AMC reinforcement. The metallic nature of the reinforcement offers better wettability than conventional covalent/ionic bonded reinforcements. With a coefficient of thermal expansion close to those of polycrystalline metals, metallic glass reinforcements exhibit lower thermal stress at the interface than ceramic reinforcements in metal matrices [7]. Al matrix composites with Cu- and Fe-based metallic glasses used as reinforcements exhibited a remarkable combination of strength and ductility [6,27]. Orowan strengthening, thermally induced dislocations, and Hall-Petch strengthening act synergistically to improve the overall strength of the composite. With most of the work focused on discussing the tensile and compressive strength, the tribological and cavitation erosion behavior of metallic glass-reinforced metal matrix composites is still an unexplored field. Due to high hardness (1341 HV) [28] of Fe-based metallic glass such as $Fe_{48}Cr_{15}Mo_{14}Y_2C_{15}B_6$, it is expected to significantly improve the mechanical properties of aluminum matrix composites.

CHAPTER II

REVIEW OF METALLIC GLASS REINFORCED ALUMINUM MATRIX COMPOSITES

Upon decades of dedicated research, metallic glasses are now used for specific applications in microelectromechanical systems (MEMS) [29], soft magnetic composites (SMCs) [30], and corrosion resistant coatings [31]. The concept of reinforcing aluminum with metallic glass is relatively new. The advantages of metallic glass reinforcement over ceramics in the metallic matrix have been discussed in the previous chapter. It turns out that metallic glasses offer a viable alternative by potentially eliminating the drawbacks of conventional ceramic reinforcement. Due to lack of thermal stability, metallic glass cannot be manufactured into larger components, and thus, have very selective applications. Lightweight metals such as aluminum and magnesium have a low melting point, and metallic glasses can find a suitable application as a reinforcement where their properties can be utilized effectively. In this section, the previous efforts made to synthesize and characterize the composites with glassy reinforcement are discussed.

2.1 Ni-based metallic glass reinforced composites

The first metallic glass reinforced Al matrix composite was synthesized and characterized by Lee *et al*. [32] in 2004. Amorphous Ni–20.6Nb–40.2Ta (wt.%) ribbons were reinforced in Al–6.5Si–0.25Mg (wt.%) alloy (Al-356) using the melt infiltration technique. The selected Ni-Nb-Ta based metallic glass exhibits high thermal stability, with a crystallization onset temperature of 720°C.

The excellent castability of Al-356 ensured the full densification of the composite during the infiltration process. Al-356 was infiltrated into the metallic glass cold compact maintained in the vacuum environment. The X-ray diffraction (XRD) analysis indicated that the metallic glass retained the amorphous structure after the infiltration process. The semi-solid processing yielded the specimens devoid of macro-scale porosity at the particle-matrix interface. Compression test was then performed on the composite samples with 20 vol.% reinforcement. In comparison with the unreinforced alloy, the composite exhibited a nearly 27% improvement in the compressive strength [32]. The increase in the mechanical properties was attributed to the high strength of metallic glass, strong interfacial bonding, and absence of interfacial products [32].

Since casting is a semi-solid or liquid processing method, it involves higher temperatures and increases the possibility of metallic glass devitrification. The metallic glass with excellent thermal stability such as Ni-Nb-Ta can retain its disordered structure at high temperature and hence is suitable for the liquid processing route. The powder processing route operates in a relatively lower temperature range and minimizes the metallic glass devitrification risk. In the research conducted by Jayalakshmi *et al*. [33], the aluminum matrix composites reinforced with 0.05, 0.15, 0.25 V_f $Ni_{60}Nb_{40}$ (at. %) metallic glass were synthesized using microwave sintering and hot extrusion. Homogeneous distribution of the particles was confirmed through the SEM images. XRD analysis confirmed the retained amorphous nature of the reinforcement after the processing. The mechanical properties of the composites were analyzed by the hardness test, compression, and tensile test. With a 25% reinforcement volume, the hardness increased by 130%. The compressive strength reported

~100% increment. While the increment in hardness and compressive strength was gradual, tensile strength only increased after a threshold of 5% reinforcement volume. The tensile properties were compared with the conventional particle/ fiber-reinforced aluminum-matrix composites. The properties were superior/ competitive with conventional composites. Good matrix-reinforcement interfacial characteristics resulted in the efficient load transfer and thereby improvement in the mechanical properties. The SEM analysis of the tensile fracture surface showed dominant ductile fracture paired with the strong interfacial bonding. Particle fracture was reported in the composite with high reinforcement content.

2.2 Ti-based metallic glass reinforced composites

A research conducted by Z. Wang *et al.* [34] discussed the effect of using Ti-based metallic glass flakes ($Ti_{48}Zr_{7.5}Cu_{39}Fe_{2.5}Sn_2Si_1$ (at. %), 15 vol.%) as reinforcement in the aluminum matrix. Broken flakes of melt-spun metallic glass ribbons were mixed with gas atomized Al7075 powder. The mixture was sintered below the glass transition temperature of the metallic glass (646 K) [35] but higher than the aging temperature of Al7075 alloy. XRD patterns (Fig. 2.1) confirmed the precipitation of thermodynamically stable intermetallic phases such as Al_2CuMg and $MgZn_2$. However, no devitrification of the metallic glass reinforcement was observed. Although the temperature was far off the super-cooled liquid region ($T_{x1} - T_g$), high densification was achieved in SPS under the influence of high pressure.

SEM and EDS micrographs confirmed the uniform distribution of the reinforcement phase in the matrix and absence of porosity or cracks at the interface. No interfacial reaction product was reported in EDS as well as XRD analysis. The addition of Ti-based metallic glass showed remarkable improvement in the compressive strength. The composite yielded at 950 MPa, which

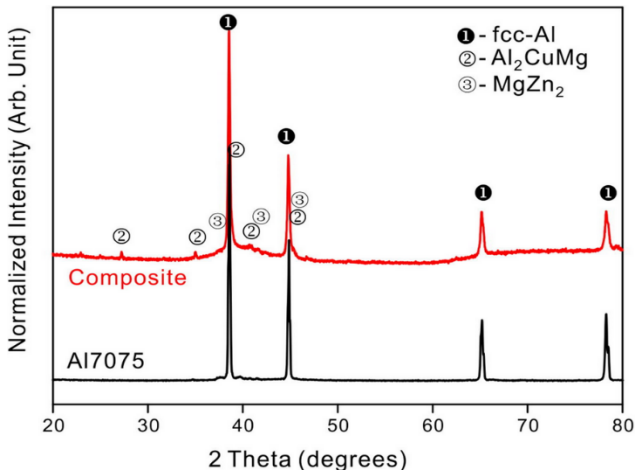

***Figure 2.1**: XRD patterns of the sintered Al7075 alloy without the reinforcement and the composite* [34]

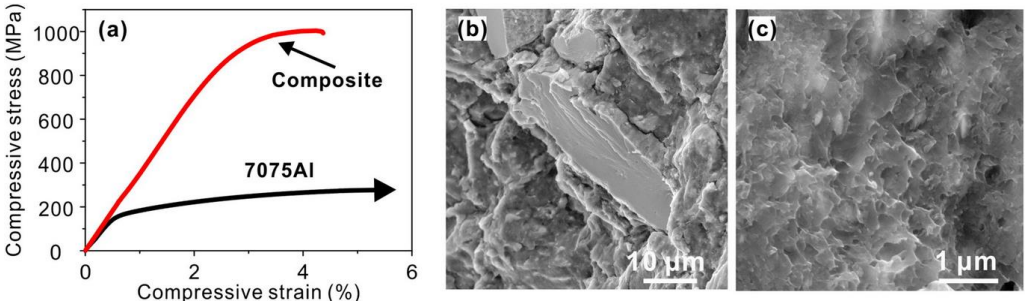

***Figure 2.2**: Compressive stress-strain curve of the composite compared with unreinforced Al7075 (a) and SEM micrographs of the fracture surface of the composite after failure (b and c)* [34]

was nearly six times higher compared to the compressive strength of unreinforced Al7075 (168 MPa), as seen in Fig. 2.2 (a). The primary mechanism of strengthening was the load transfer from the ductile matrix phase to the reinforcement phase. Strength increased dramatically at the expense of fracture strain, which dropped to 4% for composites. This was attributed to the low elastic strain limit of the metallic glass phase, which would crack under the influence of the transferred load. SEM micrograph of the fractured surface also exhibited the smooth fractured surface on a metallic glass flake while dimples on the matrix region (Fig. 2.2 (b)). The rule of mixture cannot solely explain the strength of the composite. The theoretical value of the compressive strength was

considerably lower than the experimental value. The rule of mixture only considers the direct strengthening mechanism/load transfer mechanism. Due to inadequacy in calculating the precise dislocation density, the contribution of such indirect mechanisms such as Orowan and dislocation strengthening cannot be precisely computed. Precipitates of the intermetallic compounds (Al_2CuMg and $MgZn_2$) also contributed to the strengthening. A strong interface between reinforcement and matrix prevented the particle decohesion or pullout, as can be seen on the fractured surface in Fig. 2.2 (b). Finer particles enhance the strengthening effect by offering more dislocation pile-up sites.

Ti-based metallic glasses were seen to have an excellent strengthening effect on aluminum alloys owing to their excellent mechanical properties [35]. Finer reinforcement particles impart more strength since they have less intrinsic defects than the larger/coarser particles [36]. The effect of reinforcement particles having bimodal size distribution on the Al7075 matrix was investigated by Xie *et al.* [37]. Ti-based metallic glass reinforced Al7075 composites were hot extruded at 673 K and the pressure of 590 MPa. The temperature was lower than the recrystallization temperature of the metallic glass (710 K). XRD pattern showed the presence of additional peaks other than those of pure Al, which belong to the intermetallic phases like Al_3Ti, $MgNi_2$, $TiZn_{16}$. Elements of Al7075 showed a higher affinity for the elements in reinforcement. The presence of $MgNi_2$, Al_3Ti was detected in the XRD pattern more prominently than that of Al_2CuMg, $MgZn_2$. $MgZn_2$ was the only recorded precipitate of Al7075. Usually, with the increase in the reinforcement content, the porosity increases [38]. In this experiment, however, relative density increased with reinforcement up to 6 vol.% where it reached a peak, followed by a sharp decline (Fig. 2.3). When the volume of the reinforcement was higher than the threshold of 6%, the relative density was reduced as a result of particle agglomeration. Characteristics of the interfaces were analyzed using the SEM and TEM.

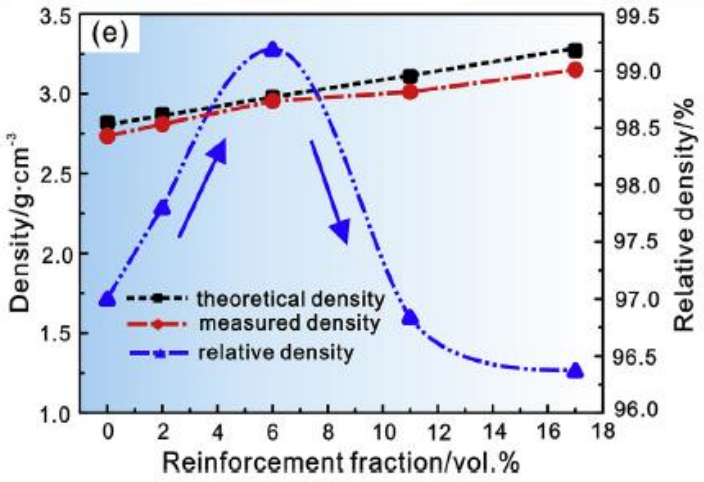

***Figure 2.3**: Variation in the relative density and density as a function of reinforcement content* [37]

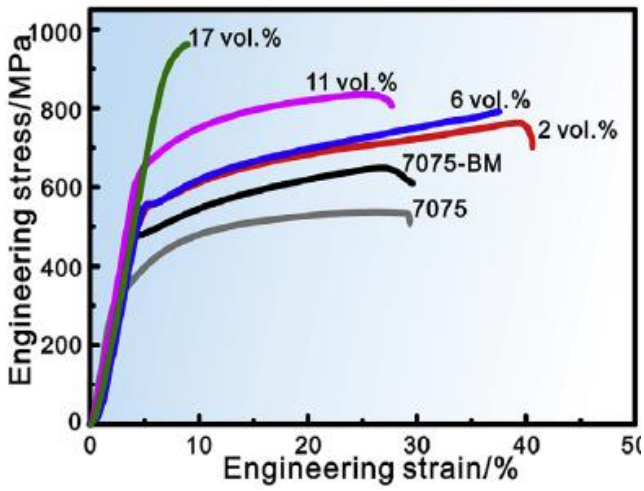

***Figure 2.4**: Compressive stress-strain curves for pure matrix material and composites reinforced with varying content of Ti-based metallic glass* [37]

As a result of atomic diffusion, a thin interfacial layer of 60-80 nm was observed. It was claimed that micro-sized reinforcement particles were partially devitrified. As a result of substantial plastic deformation during ball milling, several dislocations were found in the matrix region. Movement of these dislocations was obstructed primarily by the nano-scaled reinforcements. The highest compressive strength was recorded for 17 vol.% composite (1 GPa) at the expense of poor fracture

strain (8%). Due to local stress concentration and load transfer from the matrix, cracks were first observed in the micro-sized reinforcement. Cracks propagate through the center of the particle and not from the interface, indicating the strong interfacial bonding.

2.3 Cu-based metallic glass reinforced composites

In the study reported by Dudina *et al.* [27], heavily milled (24 h) $Cu_{54}Zr_{36}Ti_{10}$ metallic glass ribbons were reinforced in Al 520 alloy by induction heated sintering process. The stress-strain curves for the compression test revealed a remarkable increase in the compressive strength of the composite with 15 vol.% reinforcement. The strength was nearly thrice as much of that of the Al 520 alloy. The primary mechanisms involved were dislocation strengthening caused by the dislocations generated by ball milling of the pre-mixed powder and Orowan strengthening. Grain refinement (Hall-Petch effect) and solid solution strengthening of the Al-matrix by Cu diffusion from the metallic glass also contributed to the strength. The composite exhibited a good fracture strain of 13%, demonstrating an excellent combination of strength and ductility. The experimental strength values were found to be far superior to those of some conventional cast AMCs, including Al-2024/SiC_p and Al-8090/SiC_p composites. The research indicated the reliability of the powder processing/ sintering route as well as the compatibility of metallic glasses as the potential alternative reinforcement in metal matrix composites.

2.4 Zr-based metallic glass reinforced composites

The mechanical properties and deformation behavior of $Zr_{57}Ti_8Nb_{2.5}Cu_{13.9}Ni_{11.1}Al_{7.5}$ metallic glass reinforced Al-matrix were investigated by Scudino *et al.* [39]. The mechanically alloyed metallic glass powder was mixed with Al-powder followed by hot-pressing and extrusion. Experimented density values of both the composites (40% and 60% reinforcement) showed agreement with the rule of mixture, indicating the absence of macro-porosity. Due to the high reinforcement volume fraction, the grouping of the particles was observed in the optical micrographs. The composites showed a 30-70% increase in the compressive strength. The effect of particle grouping/particle

contiguity was addressed by using the shear lag model. The estimation made by the model was compared with the experimental values. The strength contributions made by Orowan stress, thermal expansion coefficient mismatch stress, and geometrically necessary dislocation stress were thoroughly analyzed. The compatibility of Zr-based reinforcement in the Al matrix was highlighted in the research. The effectiveness of the strength predicting shear lag model and self-consistent effective medium approximation (SECMA) for deformation analysis was demonstrated.

2.5 Processing of composites using spark plasma sintering

Over the years, spark plasma sintering (SPS) has evolved as the competitive powder processing route, offering excellent control over the process parameters. This technique applies pulsed direct current and uniaxial pressure simultaneously to densify the powder. The schematic of SPS and the mechanism of sintering were shown in Fig. 2.5 (a) and (b), respectively [40-41]. SPS processing has several advantages over conventional casting. Since the sintering process is entirely in solid-state, the possibility of segregation is relatively less than that for casting. The density of the final product can be controlled in SPS by controlling the processing temperature and pressure. SPS also offers advantages over other powder processing techniques such as hot isostatic pressing (HIP) [41] and hot pressing (HP) [42], by allowing low temperature and rapid sintering [43]. The presence of plasma in spark plasma sintering was a topic of debate for a long time until Hulbert *et al.* [44] claimed the absence of plasma through their research. The pulsed electric discharge causes surface activation of the powder particle. The process involves an electrical breakdown of the surface oxide layer, providing a clean surface for neck formation [45]. Current flows through the contact points of powder particles, and heat is generated due to the Joule effect. High current density and Joule heat at the neck enhances the migration of the atoms. The temperature difference between neck and particle core accelerate the neck growth. The neck is formed as a combined effect of localized

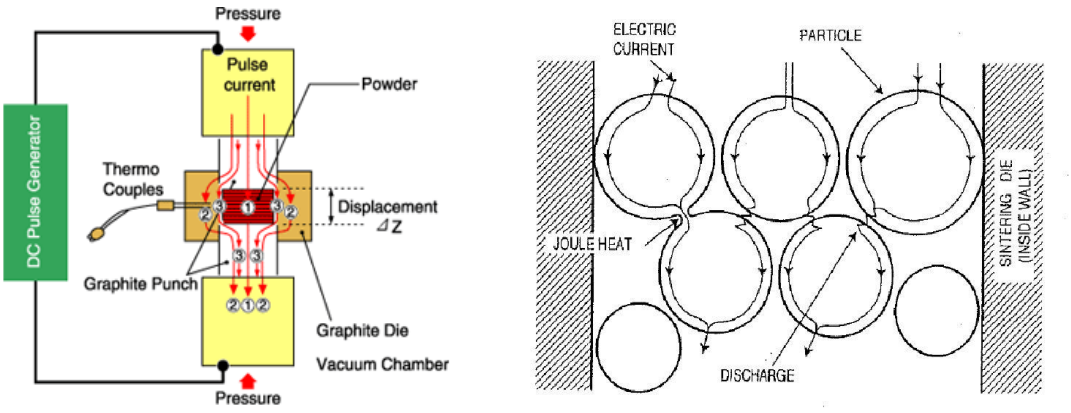

***Figure 2.5**: (a) Schematic of spark plasma sintering process* [40], *(b) Current flow through powder particles* [41]

temperature rise and uniaxial applied pressure. Rapid densification of the powdered metal can be achieved with SPS, along with the high heating rate that suppresses the grain coarsening [46]. Spark plasma sintering has great potential for synthesizing metallic glass and composites. The crystallization of thermodynamically stable phases is suppressed by controlling the process parameters. As a result, metallic glass with a larger size and complex shape can be produced while retaining its amorphous nature. SPS has been used to synthesize the metal matrix composite reinforced with the metallic glass.

Wang *et al.* [47] investigated the capabilities of the Zr- based metallic glass ($Zr_{65}Cu_{18}Ni_7Al_{10}$) as reinforcement in lightweight Al alloy. Al-Zn-Mg-Cu alloy (Al7075) was reinforced with Zr-based metallic glass fibers (15 vol.%). Strong bonding between the reinforcement and the matrix was observed, and the reason was attributed to the formation of ~3 nm thick inter-diffusion layer. The transmission electron microscopy (TEM) images showed the constituent phases that include the Al7075 matrix, amorphous reinforcement, and the intermetallic $MgZn_2$. High-resolution transmission electron microscopy (HRTEM) and selected area electron diffraction (SAED)revealed the nanocrystalline fcc-Al and amorphous phase along with the presence of $MgZn_2$. The SAED

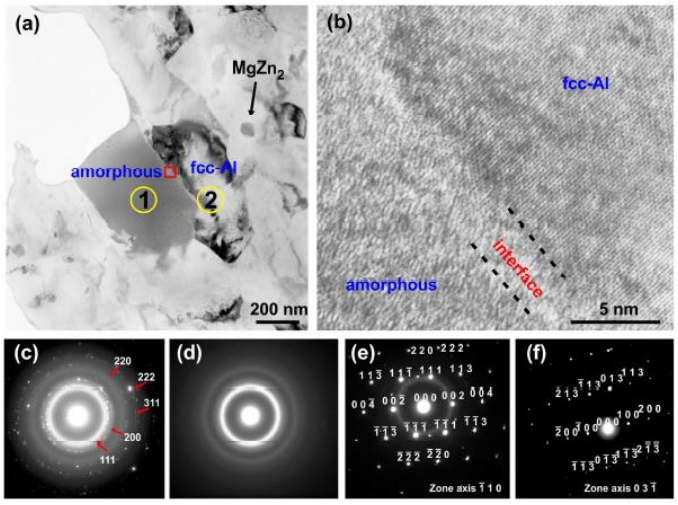

***Figure 2.6**: (a) Bright field micrograph (b) HRTEM image of the interface (c) SADF of the area corresponding to the bright field micrograph indicating nanocrystalline Al, the metallic glass and $MgZn_2$ structure* [47]

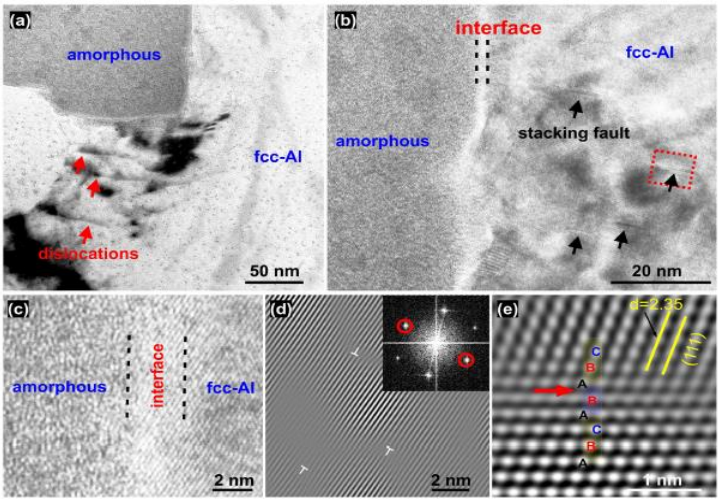

***Figure 2.7**: TEM micrographs and SAED analysis highlighting the presence of the stacking faults* [47]

pattern in Fig. 2.6 (e) confirmed the amorphous nature of the reinforcement. The SAED pattern in 2.6 (f) belonged to the η-$MgZn_2$ precipitates and the average size was measured to be 50 nm in TEM. The grain size of Al was estimated to lie in the range of 0.2-1 μm. The SAED observations in Fig. 2.7 did not show any evidence of the nucleation of an intermetallic at the interface and presence of pores. The strong bonding between Zr-based metallic glass and Al7075 in the present composite prevented the debonding of the reinforcement under the applied stress. With 15 vol.% reinforcement, the composite reported the yield strength of 366 MPa, which was twice of that of the matrix alloy Al7075 (168 MPa). TEM and SAED analysis revealed some of the strengthening mechanisms. In the TEM micrograph (Fig. 2.7 (a)), the piling of dislocations near the reinforcement particle can be seen. In addition to that, Fig. 2.7 showed the stacking faults resulting because of the secondary precipitates. The contribution of Orowan strengthening was estimated to be ~90 MPa, and it was a synergistic effect of nano-scaled reinforcement and the precipitation of the secondary phase η-$MgZn_2$. The contribution of dislocation strengthening and thermal mismatch was also calculated mathematically and was found to be 25 MPa and 75 MPa, respectively. This research exemplified the capability of spark plasma sintering as an effective processing route for metallic glass reinforced lightweight metal matrix composites.

2.6 Sliding wear

The phenomenon of surface material removal under the influence of interactions between the contacting surfaces is recognized as wear [48]. The material is removed as a result of surface friction caused by mechanical loading, vibrational damping, moving components, etc. The rate of wear is further accelerated by the presence of a corrosive environment and depletion of the lubricant layer. The majority of the mechanical systems tend to lose their durability and reliability faster due to the wear damage. Understanding the wear mechanisms and development of wear-resistant materials have become a strong necessity for the progress of advanced and sustainable machinery. Wear, in general, is a broad term. Based on the chemical and physical nature of the mating surfaces

and the surrounding environment, wear is explained by various mechanisms such as adhesive, abrasive, oxidative, and fatigue wear. As a result of frictional heating and formation of the oxidative surface layer, the material surface response is dynamic, and the dominant mechanism of wear might change. Wear generally happens through more than one mechanism. Understanding each of the modes is necessary.

Dry sliding wear is associated with a high coefficient of friction and high wear loss. The specific rate of wear is high for unlubricated condition and lies between 10^{-5} to 10^{-2} mm^3/Nm [48]. The wear rate is particularly higher in abrasive mode, where two dissimilar materials with different hardness values are sliding against each other. Frictional heat produced catalyzes the thermal reaction on the surface, forming the oxide layer. The protective oxide layer mitigates the wear rate up to a certain extent. However, the breakdown of the layer generates a large number of oxide particles that act as a third body and accelerate the wear. Archard's wear equation that correlates wear coefficient (K) with the normal load applied (W), sliding distance, volume wear loss (Q), and hardness of the material (H) is given by [49]:

$$Q = \frac{K.W}{H} \tag{2.1}$$

With the high strength and hardness, metallic glass is characterized by excellent wear resistance [50]. Hence the aluminum matrix composites reinforced with metallic glass are expected to exhibit excellent tribological properties.

2.7 Cavitation erosion

Cavitation erosion is the removal/decay of material under the influence of continuous impingement of vapor bubbles [51]. This phenomenon is common in most of the hydraulic systems such as pump turbines, ship rudders, propellers, etc. Vapor bubbles start forming when the operating pressure of fluid drops below its vapor pressure. The micro-jets and shock waves impinging with speed higher than 100 m/s cause highly localized temperature rise and pressure pulse as high as 10^3 MPa lasting

for less than 1 μs [52]. The given pressure is high enough to plastically deform the metal on a microscopic scale. Repeated bursting of such bubbles causes severe surface degradation. Fig. 2.8 shows the phase diagram of water [53]. At a constant temperature, the water is vaporized when pressure is dropped below the critical value. Cavitation is replicated by using a piezoelectric device oscillating at its resonance frequency, as seen in the schematic (Fig. 2.9). Bubbles are generated at the tip of the probe vibrating at the designated

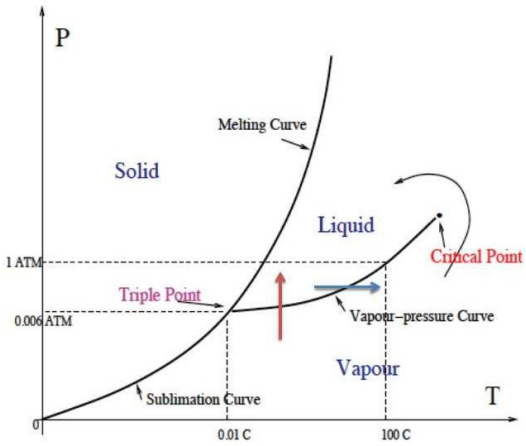

***Figure 2.8**: Phase diagram of water* [53]

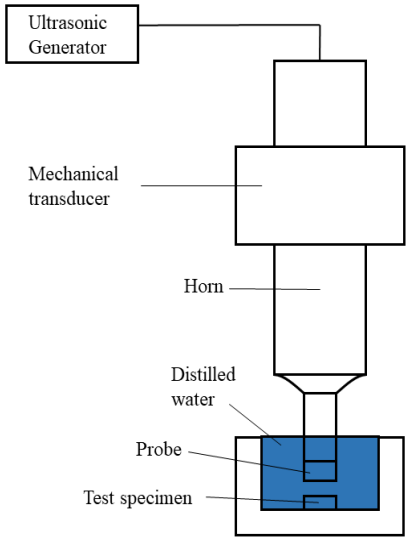

***Figure 2.9**: Schematic of cavitation erosion testing set up*

frequency and amplitude. The bubbles collapse on the sample surface, producing shock waves. In the research conducted by Vyas *et al.* [54], the average stress exerted was found to be much dependent on the distance between the tip and the sample, vibrating amplitude, and the frequency of the probe. The plot of weight loss against the separation distance showed a similar trend to that of the stress amplitude vs. separation distance. Damage due to cavitation is slow, but it's concerning since it involves stress pulses and surface fatigue. The damage is calculated in terms of Mean Depth of Erosion (MDE), which is formulated as [55]:

$$MDE = 1000.\frac{\Delta w}{\rho A} \tag{2.2}$$

where Δw is the weight loss in mg, ρ is the density in g-mm^{-3}, and A is the area affected in cm^2. The stress is sufficient to cause severe plastic deformation. It also induces residual stress and increases the dislocation density beneath the surface. The environment in which the test is conducted also influences weight loss.

The tensile and compressive properties of the metallic glass reinforced aluminum matrix composites have been widely studied. To the author's knowledge, no research has been reported that investigates the cavitation erosion properties of metallic glass reinforced AMCs. Metallic glass exhibits outstanding cavitation erosion resistance [56]. It has continuously been reported in previous researches that cavitation erosion resistance does not solely depend on the hardness and strength of the composite or the coating. In the case of composites, the weak interface between reinforcement and matrix causes debonding and reinforcement pullout under cavitation action [57]. Efforts have been made to nucleate coherent dispersoids by in-situ synthesizing [58]. It was observed that in-situ synthesizing offers better cavitation erosion resistance than conventional additive. In another research, it was concluded that AlSi/SiC composite suppressed cavitation erosion better than unreinforced AlSi [59]. A strong bond between SiC and the matrix, and better mechanical interlocking of Si-SiC clusters with the composite resist the distortion. However, the

effect of the SiC reinforcement on other Al- alloys is yet uncertain. A study claimed that the A356 alloy reinforced with 5% fine fly ash suppresses the cavitation pit growth [60]. Overall, it can be inferred that the amount of literature available to understand the cavitation erosion behavior of Al-MMCs, in particular, is very limited. A suitable reinforcement with strong bonding at the interface can put aluminum matrix composites in a better position in the domain of cavitation erosion sustaining materials. With strong interfacial bonding, metallic glass reinforced AMCs have prospects to show the improved cavitation erosion resistance.

CHAPTER III

OBJECTIVES AND EXPERIMENTAL METHODOLOGY

Fe-based metallic glasses (FMGs) exhibit high strength, hardness, and fracture toughness at the ambient temperature. The literature reviewed in the previous chapters indicates that FMG presents significant potential to be used as the reinforcement in aluminum. The current study aims at investigating the wear and cavitation erosion behavior of FMG reinforced aluminum through two distinct objectives.

3.1 Objectives

3.1.1 Objective 1: Dry sliding wear behavior of Al-FMG composites

The first objective of the present research work is to investigate the dry sliding wear behavior of Fe-based metallic glass (FMG) particulate reinforced Al matrix composites. The Al composites were processed using spark plasma sintering with the FMG ($Fe_{48}Cr_{15}Mo_{14}Y_2C_{15}B_6$) reinforcement content up to 50 vol.%. The wear behavior of the Al composites is correlated with the microstructure and mechanical properties of the composites.

3.1.2 Objective 2: Cavitation erosion behavior of Al-FMG composites

The second objective of the present research work is to investigate the cavitation erosion behavior of Fe-based metallic glass (FMG) particulate reinforced Al matrix composites. SPS sintered Al

composites with FMG reinforcement content (up to 40 vol.%) were used for this study. The effect of reinforcement content and erosion time on the surface characteristics of eroded composite microstructure, elemental composition, and surface characteristics were studied.

3.2 Experimental methodology

Materials and processing: Pure aluminum powder (98 wt.%, Alfa Aesar, 10-14 µm) and Fe- based metallic glass powder ($Fe_{48}Cr_{15}Mo_{14}Y_2C_{15}B_6$, 25-50 µm) were milled for 15 min at 150 rpm in Fritsch Pulverisette-7 high energy ball mill. This mixed powder containing varying content (up to 50 vol.%) of metallic glass was then sintered at a temperature of 550^{o}C and pressure of 70 MPa for 10 minutes at the heating rate of 100^{o}C/min in a commercial SPS system (Thermal Technology LLC, CA). Optimum sintering temperature was selected to ensure that: i) metallic glass does not crystallize, ii) aluminum does not melt, and iii) composites are nearly fully densified. Cylindrical compacts of 15 mm diameter and 3 mm thickness were sintered using graphite dies and punches. The density of pure Al and the composites was measured using the Archimedes principle. The experimental values were compared with calculated values. The density was measured experimentally using the following equation:

$$\rho_a = \frac{W_a}{W_a - W_w} \times \rho_w \tag{3.1}$$

where ρ_a is the actual density, W_a is the actual mass of specimen in air, W_w is the mass of specimen in water and ρ_w is the density of water. Samples were weighed in Mettler Toledo density meter, with the accuracy of 0.1 mg.

Polishing and hardness measurement: Samples were thoroughly polished using a Struers Tegramin specimen preparation system. Microhardness was taken with Clark microhardness tester CM-700AT at 500 g load for 15 s dwell time.

X-ray diffraction: A Phillips X-ray diffractometer was used to perform the XRD analysis. Cu-Kα radiations of wavelength 1.54 Å were generated at 45 kV voltage and 40 mA current with diffraction angle varying from 30^o to 80^o, incrementing 0.02^o 2θ with each step. XRD was done to identify phases after the sintering.

Microstructural analysis: Optical microscopy of the sintered samples was performed to visualize the reinforcement particle distribution in each sample. High resolution scanning electron microscopy was conducted using a FEI, Quanta 600 scanning electron microscope equipped with a field emission gun (FEG).

Sliding wear test: Ball-on-disc room temperature dry wear test was performed on sintered and polished composite discs at 10 N normal load, 100 rpm speed for 90 minutes (Nanovea Tribometer, Irvine, CA). Polished composite surfaces were slid tracing a circular path of 3 mm diameter against 2140 VHN silicon nitride (Si_3N_4) ball of 6 mm diameter. Wear track profiles were analyzed using the Nanovea PS50 profilometer. A reference line was drawn on each wear track profile, and the area enclosed between the reference line and wear track was calculated. The calculated area was multiplied by the circumference of the circle to measure the volume loss.

Cavitation erosion test: Cavitation erosion test was performed on all the composites and pure Al for 5, 15, and 25 min, according to the ASTM G 32-98 standard [61]. The test was conducted using a vibratory apparatus (750 Watt, Model VCX750, Sonics-VibraCell) with 20 kHz frequency and peak-to-peak amplitude of 50 µm. The compacts were immersed in distilled water during the test 1 mm separation distance between the probe tip and the sample was maintained throughout the test. Surface profiles after each test were extracted using Nanovea PS50 profilometer. The surface profiles were further analyzed to calculate the depth distribution and average penetration depth. Backscattered electron microscopy (BSE) and energy dispersive spectroscopy (EDS) was performed for a deeper understanding of the erosion mechanism.

CHAPTER IV

RESULTS AND DISCUSSION

4.1 Dry sliding wear behavior of the composite

4.1.1 Microstructure and phase analysis

Optical micrographs of Al-matrix composites reinforced with varying metallic glass content from 10 to 50 vol.% are shown in Fig. 4.1. Fig. 4.1 (a) indicates uniformly distributed Fe-based metallic glass (FMG) particles in the aluminum matrix. The mean distance between the two particles is relatively higher in the case of the Al-10 FMG composite. With an increase in the reinforcement content, particles start agglomerating and forming a continuous network. Asymmetric sickle-shaped particles with an aspect ratio higher than 1 accelerate the formation of the reinforcement network. For Al-20 FMG and Al-30 FMG composites, the reinforcement network is discontinuous, as highlighted in Fig. 4.1 (b) and (c), respectively. In Fig. 4.1 (d) and (e), the network becomes continuous for composites with higher reinforcement content (Al-40 FMG and Al-50 FMG). Spark plasma sintering of the pre-mixed composite powder at 550^{o}C with a uniaxial pressure of 70 MPa yields the near full densification of the composites. No porosity is observed in the microstructures of Al-10 FMG, Al-20 FMG, and Al-30 FMG. However, in the case of Al-40 FMG and Al-50 FMG composites, micro-porosity is observed between the reinforcement particle agglomerates where aluminum could not

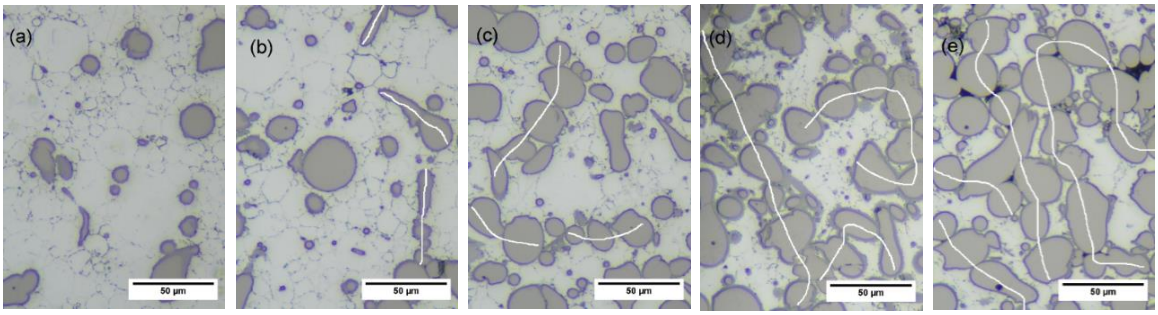

Figure 4.1*: Optical micrographs of consolidated composites (a) Al-10 FMG, (b) Al-20 FMG, (c) Al-30 FMG, (d) Al-40 FMG, and (e) Al-50 FMG. White lines are drawn manually to highlight the fiber-like arrangement of particles*

infiltrate during the sintering process. The micro-pores are observed in the AMC due to the difference in the strength of matrix and reinforcement and slightly different morphologies of the reinforcement and the matrix. A larger number of closed pores are observed as reinforcement volume is increased. This effect is prominent when matrix and reinforcement have a marginal strength and CTE difference, and it has been previously addressed [38,62].

The glass transition (T_g) and recrystallization temperature (T_{x1}) of the $Fe_{48}Cr_{15}Mo_{14}Y_2C_{15}B_6$ metallic glass is 500 and 630°C, respectively [63]. In the temperature range ($T_{x1} - T_g$), also known as super-cooled liquid region, metallic glass exhibits viscous flow behavior. Sintering temperature (550°C) is maintained at a value much lower than the recrystallization temperature T_{x1} and within the super-cooled liquid region. This mitigates the possibility of reinforcement devitrification while ensuring near full densification. In a research where the metallic glass was coated over the aluminum substrate using SPS, the sintering was performed at 590°C. It was observed that the aluminum substrate infiltrates entirely into the overlying metallic glass coating [64]. The higher temperature might eliminate the micro-porosity observed in Al-40 FMG and Al-50 FMG composites. However, the actual powder temperature is higher than the one recorded by the thermocouple [65], which might lead to the risk of metallic glass devitrification.

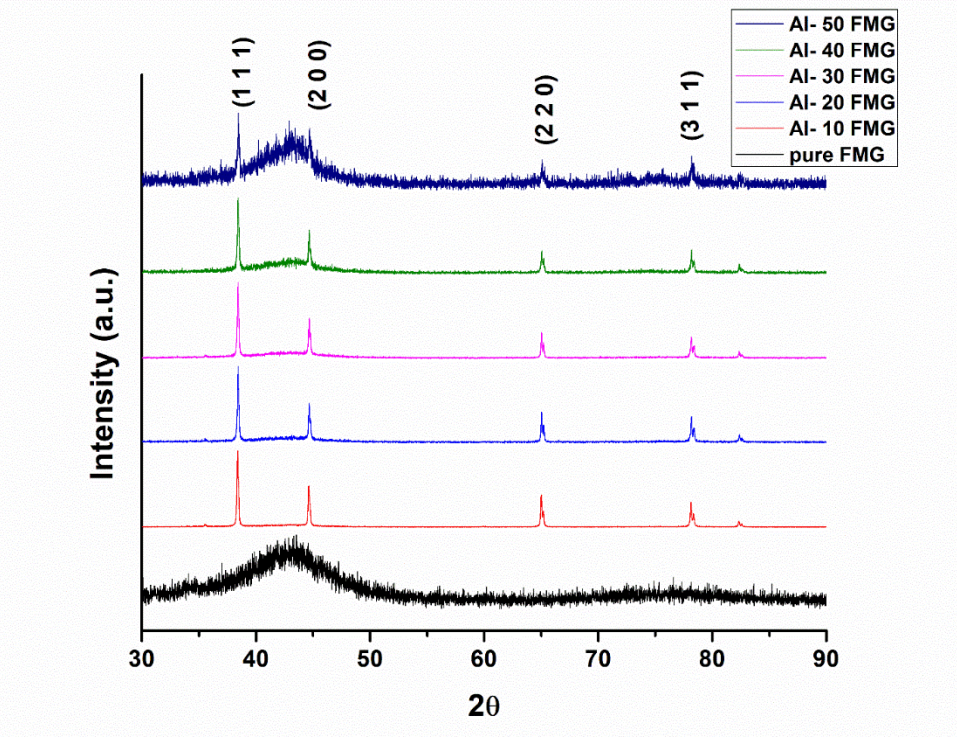

***Figure 4.2**: XRD patterns of $Fe_{48}Cr_{15}Mo_{14}Y_2C_{15}B_6$/Al composites fabricated by spark plasma sintering*

XRD patterns presented in Fig. 4.2 indicate the retained amorphous nature of the FMG reinforcement in all the composites. The broad halo at 44º 2θ suggests that FMG powder before pre-mixing is entirely amorphous. In the diffraction patterns of the composite, the intensity of amorphous halo near sharp (1 1 1) and (2 0 0) Al peaks increases gradually with increasing reinforcement content. Diffraction patterns do not indicate the presence of any third intermetallic phase. However, there is a possibility of short range atomic diffusion at the interface. EDS line scans over the interface (Fig. 4.3) show a very thin aluminum-rich interlayer, measuring about 1 µm in thickness. The steady change in the slope of the individual element's concentration at the boundary in the line scan confirms that the processing has not led to the formation of any intermetallic phase at the interface. Considering the elements in FMG, the interfacial phase can be the quasi-crystalline $Al_{91}Fe_4Cr_5$ [66].

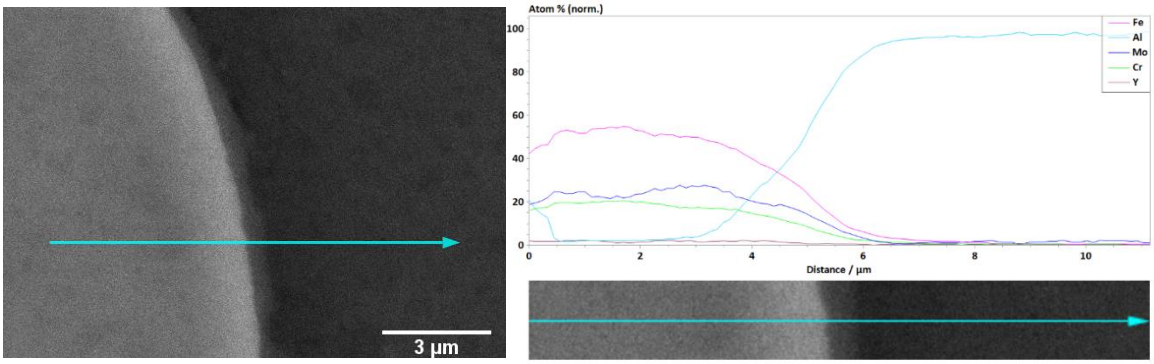

***Figure 4.3**: SEM micrograph and Elemental composition plot of the interfacial region in Al-30 FMG composite*

4.1.2 Consolidation and mechanical strength prediction

Before sintering the pre-mixed powder, densities of the composites were estimated using the rule of mixture (ROM). It is assumed that the reinforcement and matrix phase remain inert during the processing. The density of the composite is measured using the following expression:

$$\rho_C = V_m\rho_m + V_R\rho_R \tag{4.1}$$

where ρ_c is the density of the composite, and V_m and V_R are the volume fractions of matrix and reinforcement, respectively. ρ_m and ρ_R was measured to be 2.7 and 7.6 g.cc^{-1} respectively. The density of the composite is a linear function of reinforcement volume content. The experimental values coincide with the calculated values, showing agreement with the rule of mixture, as observed in Fig. 4.4. This relation holds when two

***Table 4.1**: Reinforcement weight fractions, Vickers's micro-hardness values, and volume wear rates of composites.*

Composite	Corr. wt. %	Hardness (HV)	Wear rate (mm^3/Nm)
Pure Al	-	38.25	0.615×10^{-3}
Al-10FMG	23.9	49.45	0.449×10^{-3}
Al-20FMG	41.2	64.85	0.323×10^{-3}
Al-30FMG	54.8	81.86	0.234×10^{-3}
Al-40FMG	65.0	458.03	0.116×10^{-3}
Al-50FMG	73.6	752.20	0.039×10^{-3}

constituents do not react with each other and contribute separately to the total density value. The change in the hardness values cannot simply be explained by the rule of mixture. Hardness varies linearly up to 30 vol.% reinforcement, followed by a sudden increase (Fig. 4.5). Strength and hardness are roughly correlated by the relation $H_v \approx 3\sigma_{UTS}$ where σ_{UTS} is the ultimate tensile strength [67]. ROM would not be the right criterion to predict the yield strength. In particle reinforced AMC, it has previously been observed that yield strength does not vary linearly with reinforcement volume content [39]. With an increase in the volume, reinforcement

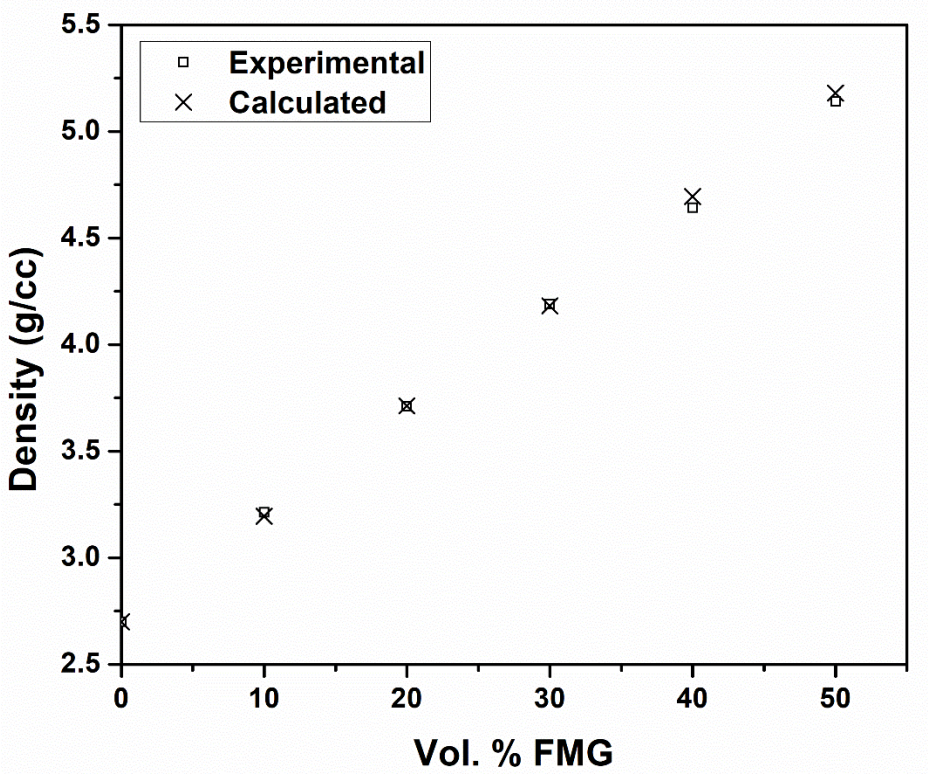

***Figure 4.4**: Calculated and experimental density as a function of FMG reinforcement content*

particles tend to form an interconnected network. The network density increases from 10 vol.% to 50 vol.% of the FMG reinforcement. The deformation mechanism changes with the changed reinforcement morphology from particle to fiber-like particle network. The shear lag model takes this change into account and estimates yield strength of the composite, σ_y with the following equation [68].

$$\frac{\sigma_y}{\sigma_m} = f\left(\frac{E^p}{E^m} - \frac{E^p - E^m}{E_m}\left(\frac{\tanh(\gamma s)}{\gamma s}\right)\right) + (1 - f) \tag{4.2}$$

where σ_m is the yield strength of the matrix, f is the reinforcement volume fraction, E^p is the elastic modulus of particle reinforcement (210 GPa [28]), E^m (70 GPa [69]) is the elastic modulus of the matrix material, s is the aspect ratio of the reinforcement particles. γ is the function of E^m, E^p, Poisson's ratio, and f and is given by:

$$\gamma = \sqrt{\frac{2E^m}{E^p(1+\vartheta_m)\ln\left(\frac{1}{f}\right)}} \tag{4.3}$$

where ϑ_m is the Poisson's ratio and is considered to be 0.33 for metals. Fig. 4.1 highlights the fiber-like arrangement of particles. The particles are widely distributed in the Al-10 FMG composite. Short and discontinuous networks start appearing in Al-20 FMG and Al-30 FMG composites. Usually for reinforcements with spherical morphology, the network formation and sudden increase in the strength was observed after 50 vol.% reinforcement [70]. It is the threshold beyond which a larger number of particles come in contact with each other. However, in this case, that threshold appears to have been shifted to 30 vol.%. The hardness of the composite varies almost linearly up to 30 vol.%, followed by a sudden upsurge in 40 vol.%. Interestingly, the calculated yield strength ratios based on the shear lag model show a similar trend as that of the hardness (Fig. 4.5).

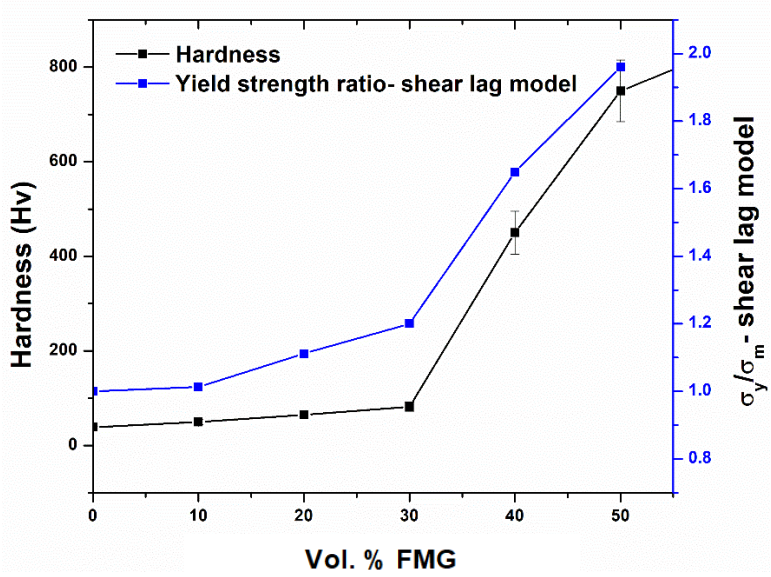

***Figure 4.5**: Hardness and the calculated ratio of yield strength of composite to matrix as a function of FMG reinforcement content*

However, this calculation needs experimental validation through compression or tensile testing. Assuming the strength-hardness dependence to be true, shear lag model theoretically and mathematically explains the sudden rise in the hardness after the threshold of 30 vol.% FMG reinforcement.

4.1.3 Wear analysis

Fig. 4.6 represents 2-D wear profiles of the specimens after being subjected to the dry sliding wear for 90 min. Pure Al shows maximum wear depth (35 µm), and the wear depth decreases with an increase in the reinforcement content. From the wear profiles of Al-30 FMG, Al-40 FMG, and Al-50 FMG, it is observed that the grooves formed have a non-uniform morphology. In the beginning, the silicon nitride ball makes a curved contact with the specimen, and the surface gets ploughed during sliding. Parallel grooves appear on the surface as a result of abrasive wear and are identified with SEM

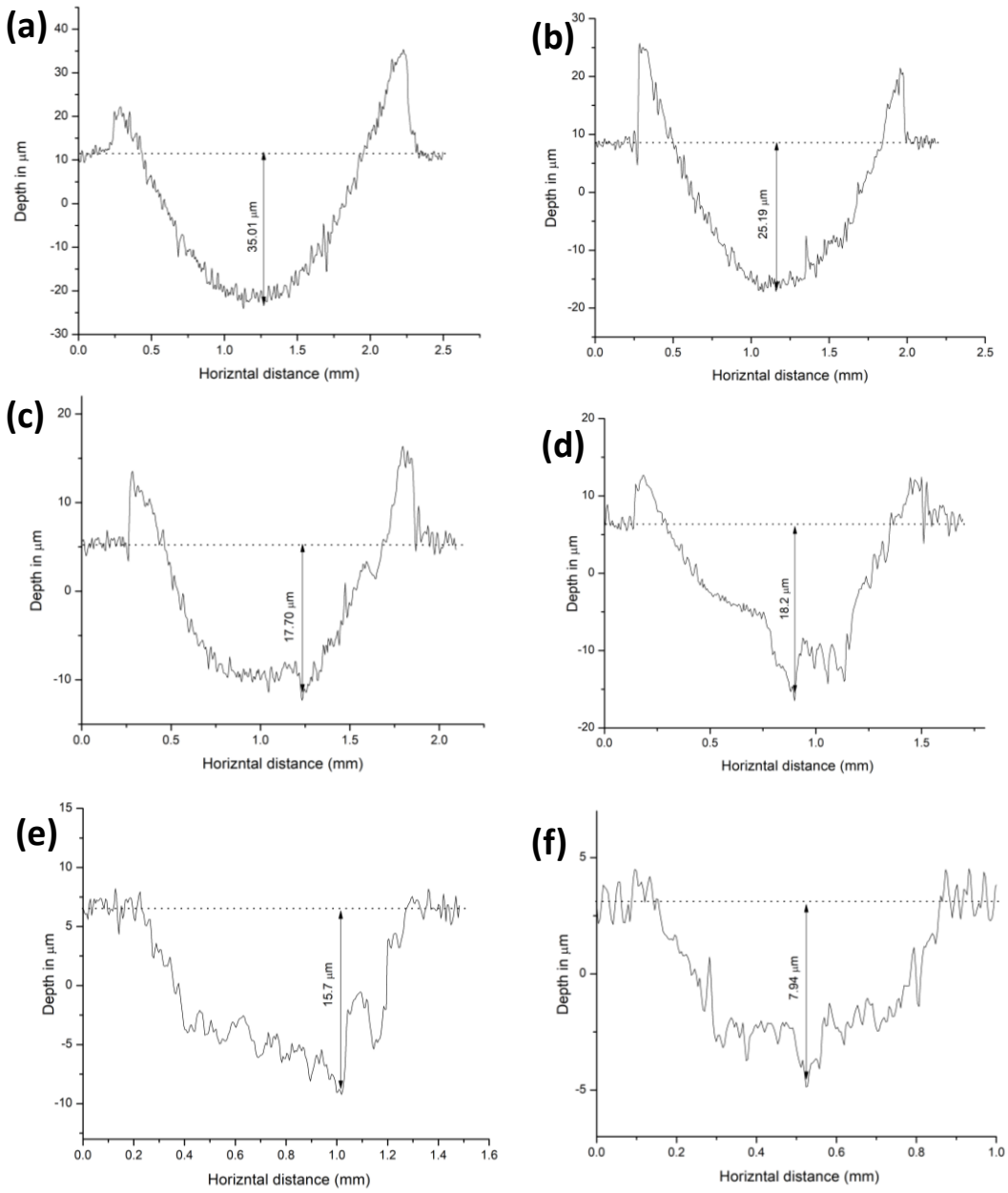

Figure 4.6*: Wear depth profiles of (a) pure Al (b)Al-10 FMG, (c)Al-20 FMG, (d) Al-30 FMG, (e) Al-40 FMG, and (f) Al-50 FMG composites*

micrographs. In the case of pure Al and the composites with low reinforcement content (Al-10 FMG, Al-20 FMG), a wedge-like wear particle [48] of ductile aluminum forms ahead of the Si_3N_4 ball. With repetitive sliding, the wedge builds up by clogging aluminum from the surface and enlarging the groove. The plastic flow of aluminum causes leads to the formation of ridges on both

sides of the groove. Reinforcement particles resist the degree of ploughing and plastic deformation of aluminum, which is anchored by the firm, adherent, and uniform interlayer between the metallic glass particles and the matrix. The particles wear continuously with the matrix as a result of a strong interlayer. Once the interlayer fractures, the particle detaches the matrix and contributes to the three-body abrasion. Such cases, however, are infrequent and rarely observed in the current study. In Al-40 FMG and Al-50 FMG composites, multiple continuous reinforcement networks and loops emerge as a result of particle contiguity, and the deformation mode shifts from ploughing to ideal material removal. As a result, the plastic deformation of aluminum is heavily suppressed by the reinforcement networks, and no ridges are formed on either side of the groove. Metallic glass particles end up either fracturing or detaching from the matrix surface as a result of their brittle nature.

Degree of wear (β) is a function of the groove volume ΔVg, and the ridge volume ΔVr and calculated by the following equation [48].

$$\beta = \frac{\Delta Vg - \Delta Vr}{\Delta Vg} \tag{4.4}$$

In the case of ideal material removal, ridges do not form and β = 1 while for ideal ploughing, there is no material loss and β = 0. Values of β are calculated by analyzing the wear profiles and plotted in Fig. 4.7. The value is almost constant (0.86-0.87) for pure Al, and the composites up to 30 vol.% metallic glass and jumps to 1 in Al-40 FMG and Al-50 FMG composites. The corresponding groove volume ΔVg (mm^3) is also plotted in the same graph. The trend observed is in agreement with Archard's rule of the inverse relation between hardness and wear volume loss. For metallic materials, the distribution of specific wear rates in sliding contact under lubrication conditions are summarized [48]. The value of β is related to the abrasive wear coefficient K_{ab}. For applied load W (N), total sliding distance L (mm) and hardness H ($N.mm^{-2}$), the wear coefficient K_{ab} is given by [48]:

$$K_{ab} = \beta.\frac{\Delta V g.H}{WL} \quad (4.5)$$

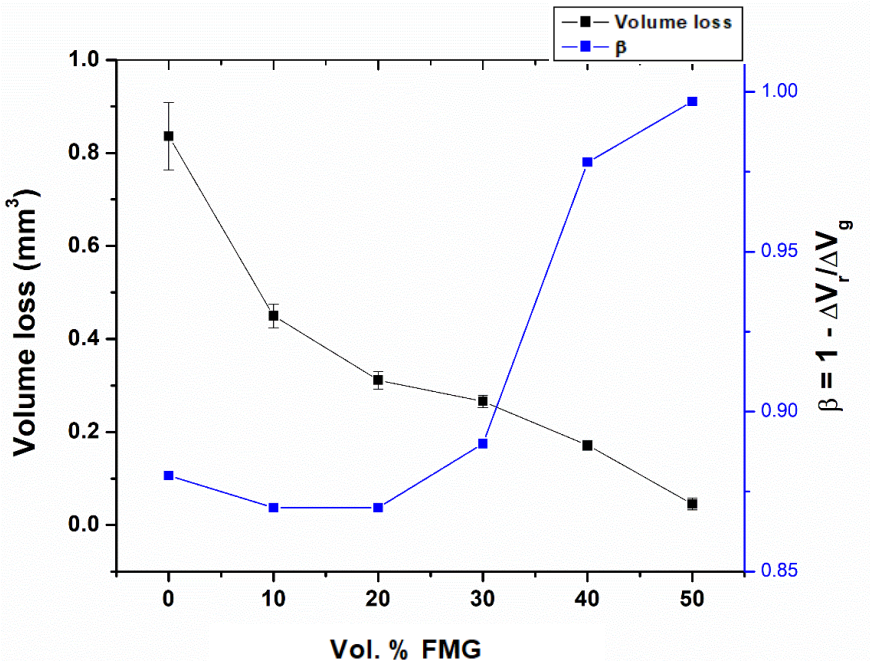

***Figure 4.7**: Volume loss and degree of wear as a function of FMG reinforcement content*

The value of K_{ab} for all the cases is in between 0.002 to 0.004, and lies well in the abrasive wear coefficient range of metals (10^{-4} to 10^{-1})[48]. In addition to that, the specific wear rate lies in the domain of abrasive wear (10^{-5} to 10^{-3} mm^3/N.m.). The specific wear rate is calculated based on the groove volume loss. Table 4.1 also gives the account of hardness and the specific wear rate variation with the reinforcement content.

The SEM micrographs of the wear surfaces are shown in Fig. 4.8. Abrasive wear grooves are seen on the smooth wear surface of pure Al (Fig. 4.8 (a)). Al-10 FMG, Al-20 FMG, and Al-30 FMG show heavily textured and non-uniform wear surface, as seen in Fig. 4.8 (b), (c), and (d). Upon the multiple passes of Si_3N_4 ball, the metallic glass particles tend to disintegrate and get dispersed into ultra-fine fragments of approximately 1 µm size. Some of them can be detected in the white dotted circles in Fig. 4.8 (d), and (e). Due to the strong interfacial bonding,

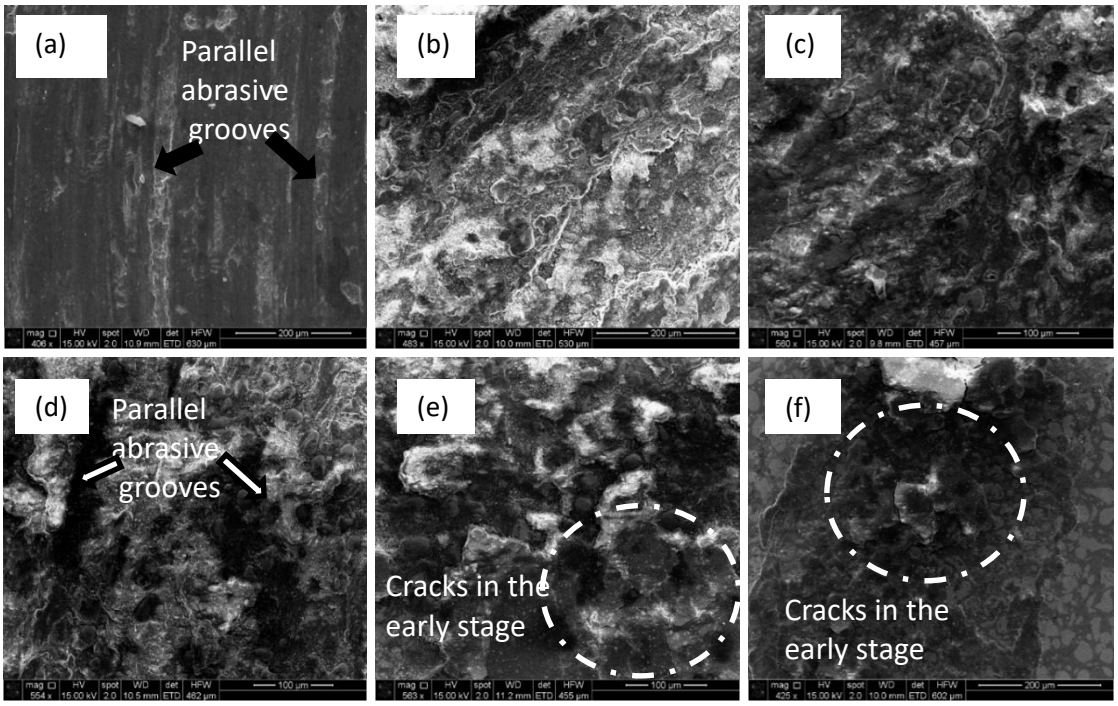

***Figure 4.8**: SEM images of the wear profiles of (a) pure Al (b) Al-10FMG (c) Al-20FMG (d) Al-30 FMG (e) Al-40 FMG, and (f) Al-50 FMG. Abrasive grooves and surface cracks highlighted.*

metallic glass particles adhere to the matrix and effectively resist the erosion. As discussed previously, particles get detached and cause three-body wear in very few cases. The most reasonable explanation for the particle debonding can be the high stress concentration at the micro-porosity sites observed in the microstructure. With an increase in the reinforcement content, the plastic deformation of aluminum is suppressed. The ideal material removal mechanism involves the initiation and propagation of the cracks primarily through the brittle interconnected particle network, as seen in Fig. 4.8 (e) and (f).

The EDS elemental maps from worn surfaces of Al-10 FMG, Al-30 FMG, and Al-50 FMG composites are presented in Fig. 4.9. Two distinguishable phases with uneven matrix surface and relatively smoother reinforcement particles are visible in the SEM micrographs. Particle surfaces show the uniform distribution of Fe, Cr, and Mo. Apart from the region where particles are visible, these elements are recorded all over the worn surface in the SEM micrograph. It happens

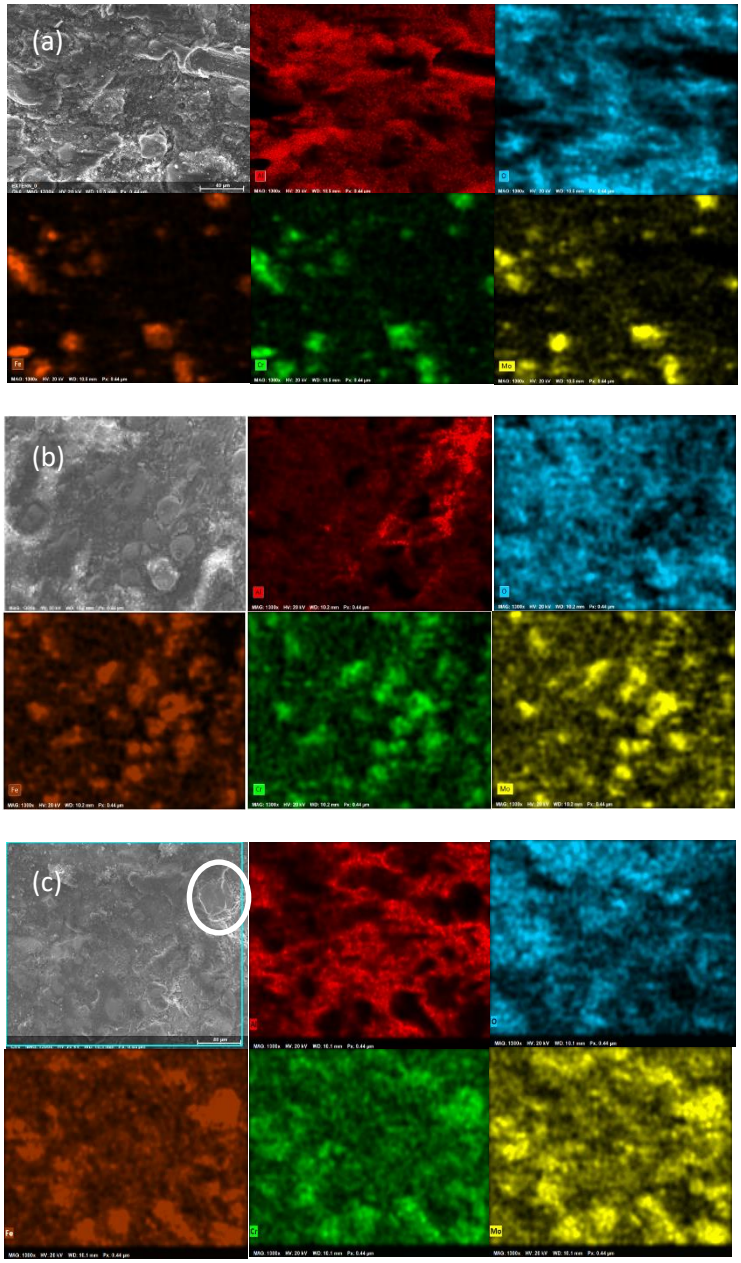

***Figure 4.9**: EDS elemental maps from the worn surfaces of (a) Al-10 FMG (b) Al-30 FMG, and (c) Al-50 FMG (fractured portion highlighted in white circle)*

mostly because of the presence of very fine particles of size >5 µm. For dry sliding under the given applied load, the larger particles fracture because of their brittle nature and deposit all over the wear track. The intensities of Fe, Cr, and Mo increases gradually in Fig. 4.9 (a), (b) and (c). This indicates

that the amount of fractured metallic glass particles on the worn surface increases with reinforcement addition. Since the larger particles have a higher probability of having intrinsic flaws and defects, they are vulnerable to early fracture. Oxidation of Fe-based metallic glass during wear is well-known and has been reported previously [63]. However, oxygen has selectively attacked aluminum to a greater extent than the reinforcement. The sliding motion causes frictional heating and leads to the formation of thin oxide layers. As the worn-out surface is rough, the oxide layer formed is not of uniform thickness and exists in fragments. Aluminum deforms plastically and covers the wear track and reacts readily with atmospheric oxygen. In the EDS elemental maps, oxygen has occupied most of the area, but its intensity is not constant throughout the area because of the non-uniform oxide layer thickness.

4.2 Cavitation erosion behavior of the composite

4.2.1 Microstructure

The previous study discussed the X-ray diffraction patterns of the starting FMG powder and composite compacts before testing them for cavitation. The sintering temperature is maintained in the supercooled liquid region (SCLR), i.e., between the glass transition temperature ($T_g = 500°C$) and the first recrystallization temperature ($T_{x1} = 630°C$) of the FMG ($Fe_{48}Cr_{15}Mo_{14}Y_2C_{15}B_6$) [63]. The amorphous nature of the reinforcement is retained during the sintering process. The heating rate and the dwell time of the process have a crucial role in suppressing the crystallization of FMG. The XRD patterns do not exhibit the presence of any intermetallic phase, as discussed in the previous study. Cavitation erosion depends mainly upon the surface conditions of the material. Fig. 4.10 shows the BSE images of the composites with 10 to 40 vol.% of FMG reinforcement. From the previous research [64], it was confirmed that >99

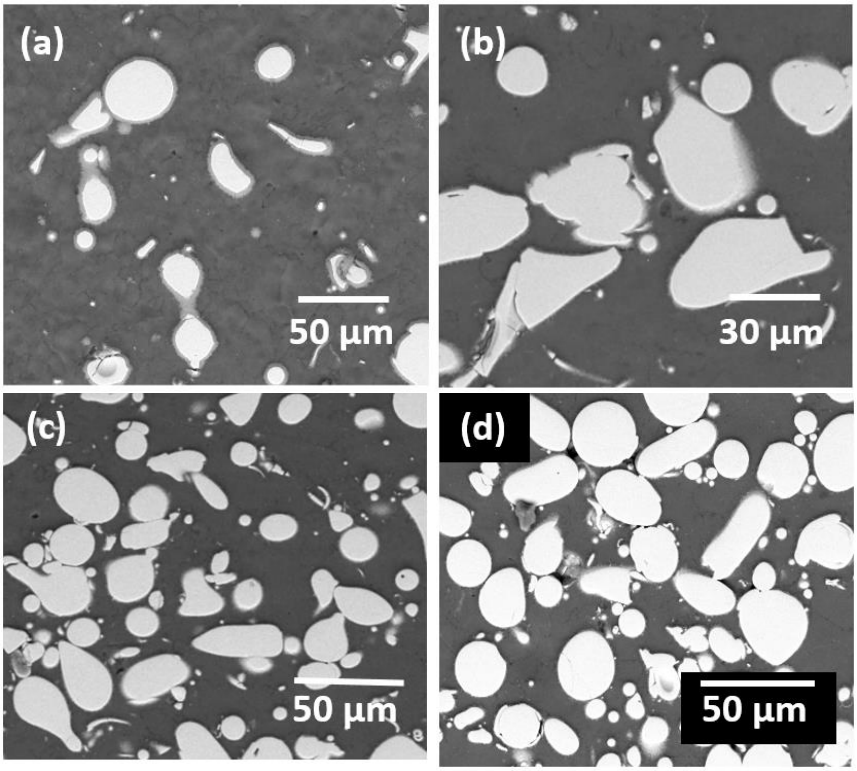

Figure 4.10*: Backscattered electron micrographs of the consolidated composites (a) Al-10 FMG, (b) Al-20 FMG, (c) Al-30 FMG, and (d) Al-40 FMG*

percent densification is achieved by sintering the powder mixture at 550ºC at 70 MPa. An increase in the reinforcement content results in the particle contiguity that is a higher number of FMG particles appending to form a continuous reinforcement network. For the composite with 40 vol.% FMG, micro-porosity is detected at specific locations, especially where the particles are agglomerated, and aluminum could not infiltrate into the entrapped voids.

The interfacial layer surrounding the reinforcement particles indicates the possibility of reaction between the matrix Al and the elements from FMG (Fe, Cr, and Mo) at the given temperature. BSE images for all the composites exhibit the interface. At certain locations (Fig. 4.10 (a)), the interfacial layers of the closely spaced reinforcement particles are merging. Merging of the interfaces enhances the formation of the reinforcement network. To better understand the elemental distribution, EDS point scans are performed on the reinforcement phase, interface, and the matrix phase. Results suggest the migration of atoms at the contact surface. As seen in Fig. 4.11, the concentration of aluminum at the interface is marginally higher than the elements from the

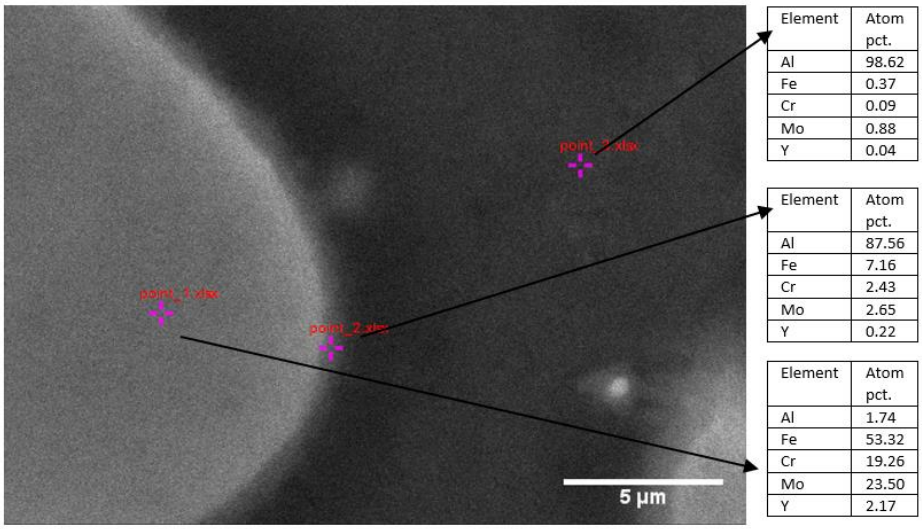

Element	Atom pct.
Al	98.62
Fe	0.37
Cr	0.09
Mo	0.88
Y	0.04

Element	Atom pct.
Al	87.56
Fe	7.16
Cr	2.43
Mo	2.65
Y	0.22

Element	Atom pct.
Al	1.74
Fe	53.32
Cr	19.26
Mo	23.50
Y	2.17

Figure 4.11*: Elemental composition on the reinforcement, the interface, and the matrix region of Al-30 FMG*

reinforcement. It can be attributed to the higher diffusivity of aluminum at the given temperature. However, there is no evidence to state the nature of the interface in terms of crystallinity and atomic order. Considering the elements in FMG, the interfacial phase can be the quasi-crystalline $Al_{91}Fe_4Cr_5$ [66]. Preferential segregation of any particular element at the interface is not detected. No porosity is identified at the interface.

4.2.2 Cavitation erosion behavior

Fig. 4.12 represents the matrix of cavitation profiles of pure Al and all the composites tested for 5, 15, and 25 min. From the profiles, it is observed that most of the area in pure Al is heavily eroded. For a 5 min test, the majority of the peripheral area is damaged. The color maps indicate that the average penetration reduces with the metallic glass addition. A relatively larger area is affected by erosion in 15 min test. The central region is observed to get equally affected as the peripheral area. For the 25 min test, the deformation zones in pure Al are distributed uniformly over the entire wear

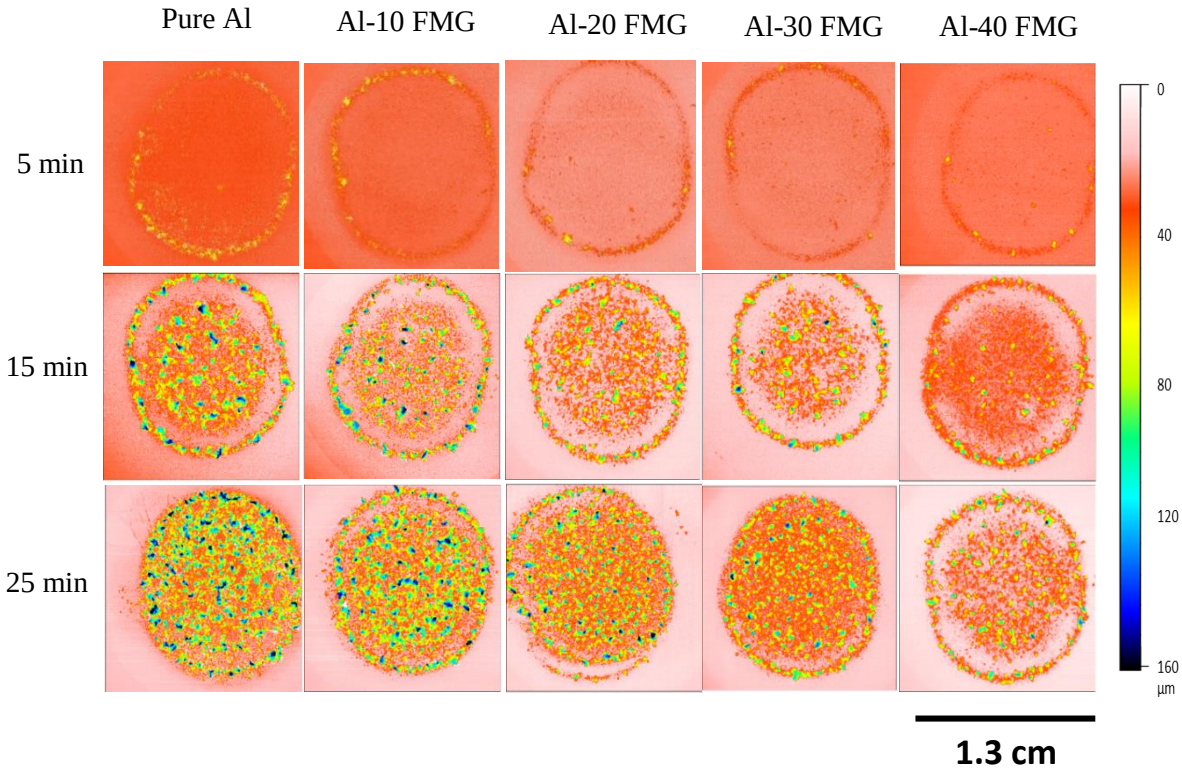

***Figure 4.12**: Worn out areas of all the composites scanned with the profilometer*

mark. Whereas towards the extreme, the profile of Al-40 FMG shows non-uniform surface profile and shallower penetration depth. Non-uniformly scattered depth profiles representing deeper penetration, with almost a quarter of the area (~ 26%) mildly affected or unaffected. With time, erosion of the surface progresses radially outwards from the center towards the periphery of the wear mark. The profiles in Fig. 4.12 shows the evolution of the wear mark on the surface of pure Al and composites with time.

For a 5 min test duration, only the peripheral portion is damaged, and the rest of the surface is hardly affected. The central area then gets eroded, followed by the radially outward progress. After 25 min of cavitation, the uniform distribution is observed on the wear mark except for Al-30 FMG and Al-40 FMG composites. This phenomenon of severe peripheral distortion in the initial stage of cavitation had been reported previously [58]. The pressure difference at the periphery is lower than the pressure at the center. It eases the bubble formation at the periphery, resulting in the early damage. More prolonged exposure is required to get a uniform deformation on the surface of Al-30 FMG and Al-40 FMG. Fig. 4.13 (a) shows the average depth of penetration for aluminum and the composites for different time intervals. Erosion depth increases linearly with time, and composites exhibit superior erosion resistance compared to pure Al. Higher relative area occupancy by reinforcement leads to higher surface hardness. With the increase in the reinforcement content, the slope of the graph decreases. The plots for composites, as well as pure Al, resemble straight lines with a constant slope. It suggests that the rate of erosion is constant until 25 min. The effect of the reinforcement is observed to be prominent at longer test durations. The average depth value for pure Al continues to drift further away from those of the composites. The resistance of the Al-40 FMG composite is marginally higher than the rest. Reinforcement networks formed as a consequence of particle contiguity resist material removal. Fig. 4.13 (b) represents the volume loss trend for all the composite calculated directly from the weight loss. In general, the

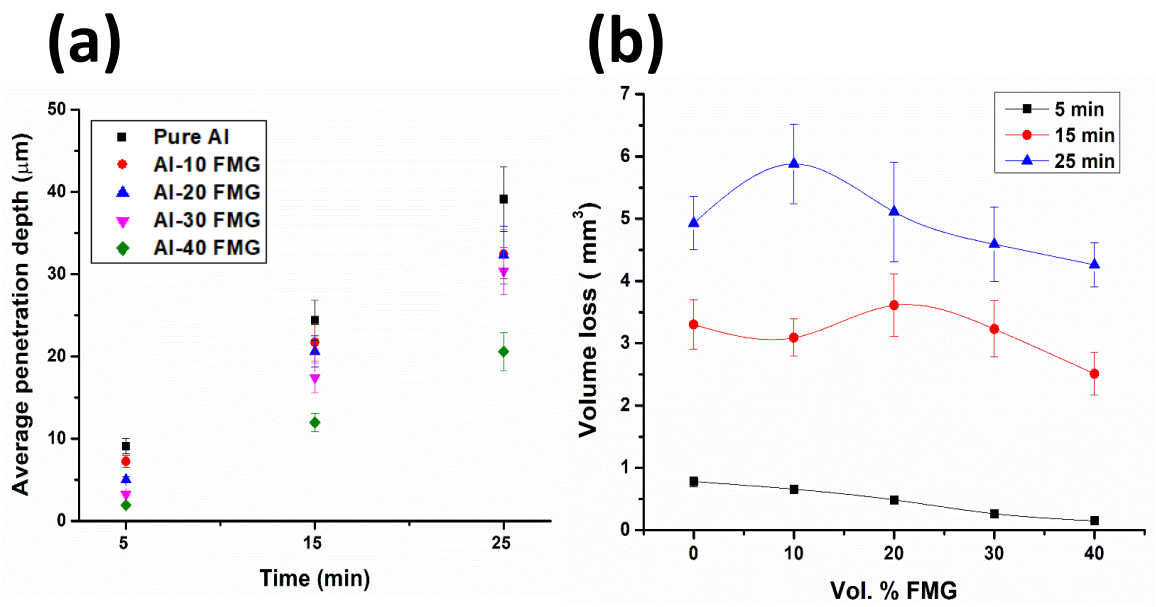

***Figure 4.13**: (a) Average depth of penetration vs exposure time. (b) Measured volume loss of the specimens as a function of FMG reinforcement content*

FMG particles inhibit the surface damage during the cavitation. Aluminum being ductile gets piled up during the erosion and remains on the surface, contributing to the overall weight of the sample. It adds error in volume loss measurements, which can't be calculated precisely due to the irregular and intricate geometry of the wear mark.

For a better understanding of the deformation caused by the cavitation erosion, the profilometer scan images are further analyzed to extract the depth distribution data by separating the identical colored clusters (Fig. 4.14). The relative area occupied by respective color clusters is assigned to the corresponding penetration depth values. Stack bars in Fig. 4.15 shows the depth distribution for composites in three sets of time intervals. For simplicity, penetration depths are divided into 5 clusters of <5 μm, 5 – 30 μm, 30 – 60 μm, 60 – 90 μm, and 90 – 120 μm. For 5 min test, none of the samples were eroded deeper than 60 μm. Most of the deformation lies between 0 – 30 μm.

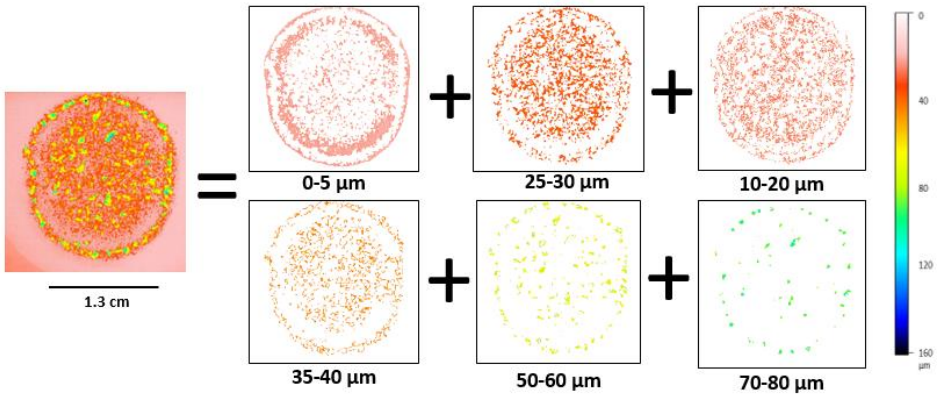

***Figure 4.14**: Disintegrating the wear profile of Al-20 FMG into clusters*

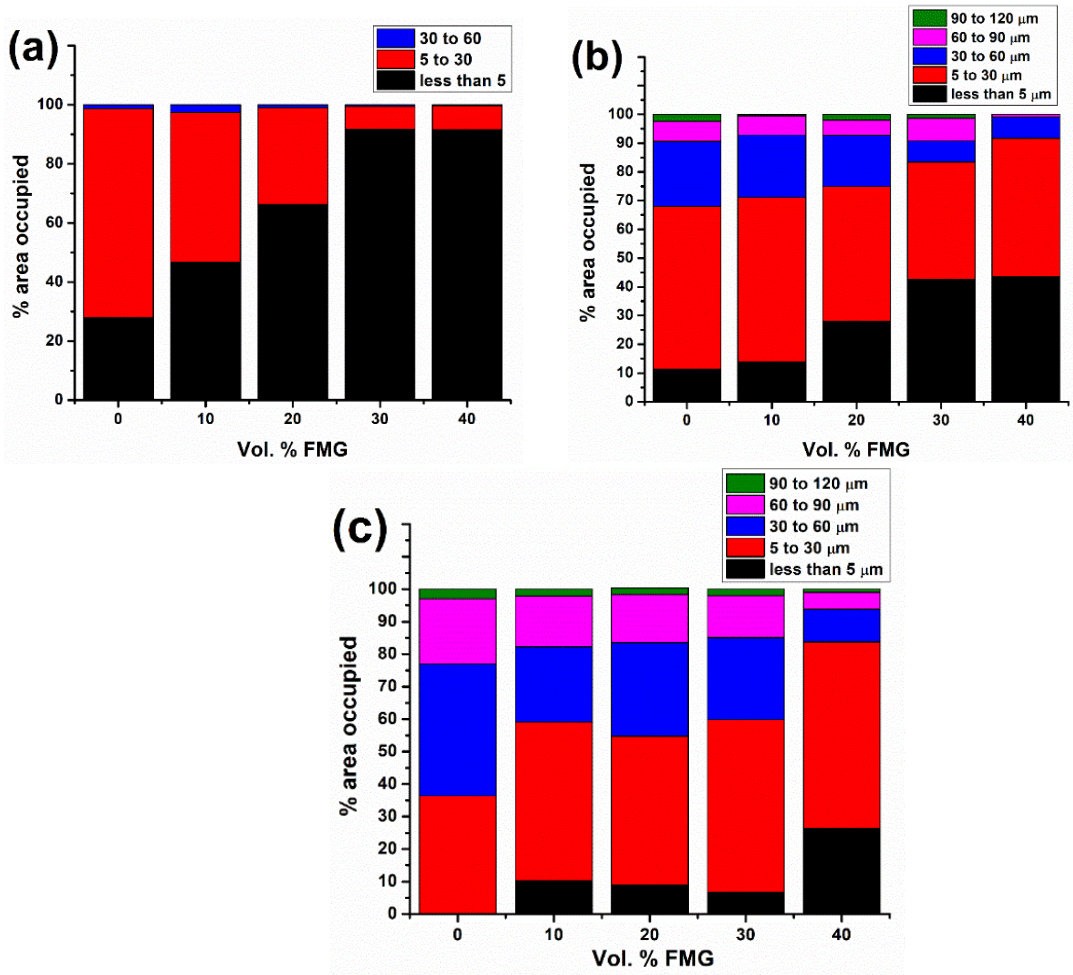

***Figure 4.15**: Area occupancy of several depth clusters after exposing the specimens for (a) 5 min, (b) 15 min, and (c) 25 min*

Around 90% of the surface of Al-30 FMG and Al-40 FMG is mildly damaged, with erosion depth less than 5 µm. For pure Al, approximately 75% of the surface is eroded in the range of 5 – 30 µm. Area occupancy of this cluster decreases with an increase in the reinforcement volume fraction. Area occupancy of the 30 – 60 µm cluster seems negligible compared to the remaining two clusters and is observed primarily at the peripheral region of the wear mark. However, this cluster is seen to occupy a sizable area in all specimens for 15 min test. The overall trend is similar to what observed in 5 min test. The mildly affected area is lower for all samples compared to 5 min test, but it increases gradually from 11.37% for pure Al to 43.5% for Al-40 FMG composite. The area occupied by 30 – 60 µm cluster reduces from 22.6% for pure Al to 7.4% for Al-40 FMG. This observation confirms that the reinforcement phase resists the distortion, and the resistance is directly proportional to the reinforcement content. In the case of Al-10 FMG and Al-20 FMG composites, the reinforcement area occupancy is lower, and the particle contiguity network is discontinuous, leading to the lower erosion resistance. For 25 min test duration, 60 – 90 µm cluster occupies 22% of the surface in pure Al, reducing to 5% for Al-40 FMG. For the 15 and 25 min bars, it appears that the <5 and 5 – 30 µm cluster size occupancy reduces with the time. The reduced area of these clusters is occupied by deeper penetration clusters. Pure Al, after 25 min, shows zero area occupancy for <5 µm deformation. It can be claimed that the surface deformation kinetics show a strong dependence on the surface conditions.

4.2.3. Erosion mechanism

Fig. 4.16 shows the SEM images of the specimen surface after being exposed to cavitation. Pure Al, due to the uniform homogeneous phase undergoes uniform distortion. In the case of composites, the matrix region is preferentially attacked. Red dotted lines highlight the particle network, which gets denser and continuous with the addition of reinforcement particles. With 10 vol.% reinforcement, the network is broken while in the case of 20 vol.% reinforcement, some closed loops are observed.

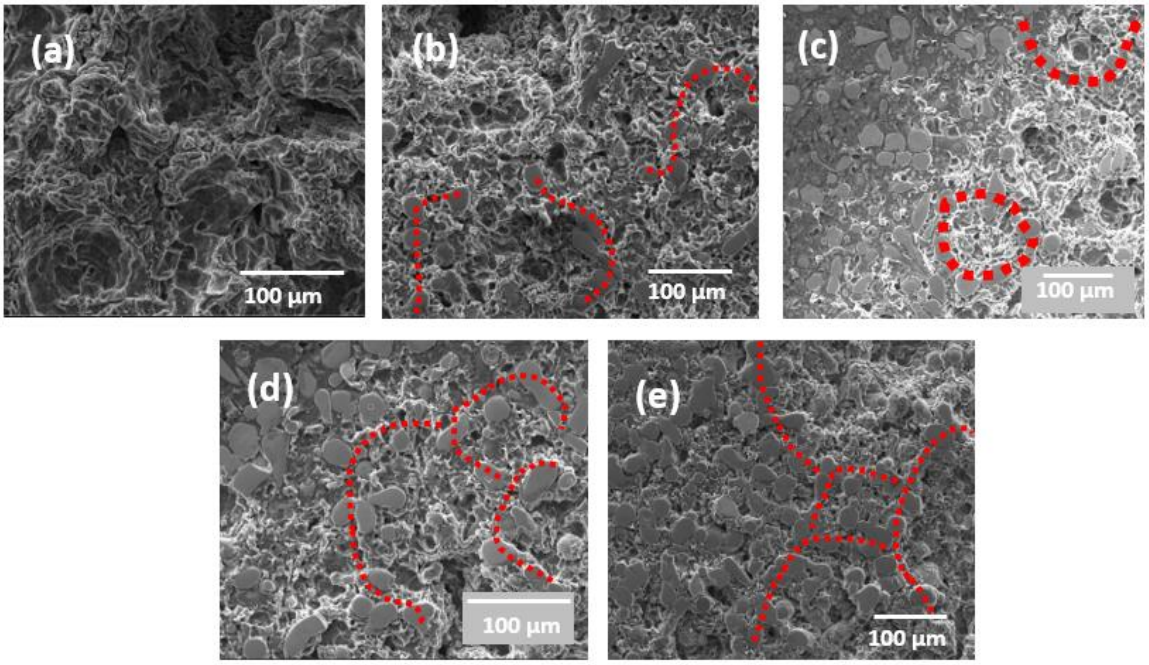

Figure 4.16*: SEM micrographs of (a) pure Al, and the composites (b) Al-10FMG, (c) Al-20 FMG, (d) Al-30FMG, and (e) Al-40 FMG after being exposed to the cavitation for 15 min Reinforcement network highlighted with dotted red lines*

The density of the network and the number of closed loops increases further for 30 vol.% and 40 vol.% reinforcement. The closed loops act as a hard and adherent boundary enclosing softer aluminum. The shock waves originating from the bursting of bubbles and water jet impingement creates surface fatigue condition on the exposed area. Aluminum, being vulnerable to the plastic deformation, undergoes early failure. The collapse of the bubbles produces localized pressure waves which develop craters by pushing the matrix material radially outwards. Aluminum clogs up with time developing localized ridges and eventually joins the debris. The SEM micrograph of pure Al suggests the mode of failure to be ductile tearing [71]. For brittle metallic glass particles, the deformation mechanism is different than the matrix. In the BSE image of eroded Al-10FMG composite (Fig. 4.17), reinforcement particles are seen to exhibit brittle fracture.

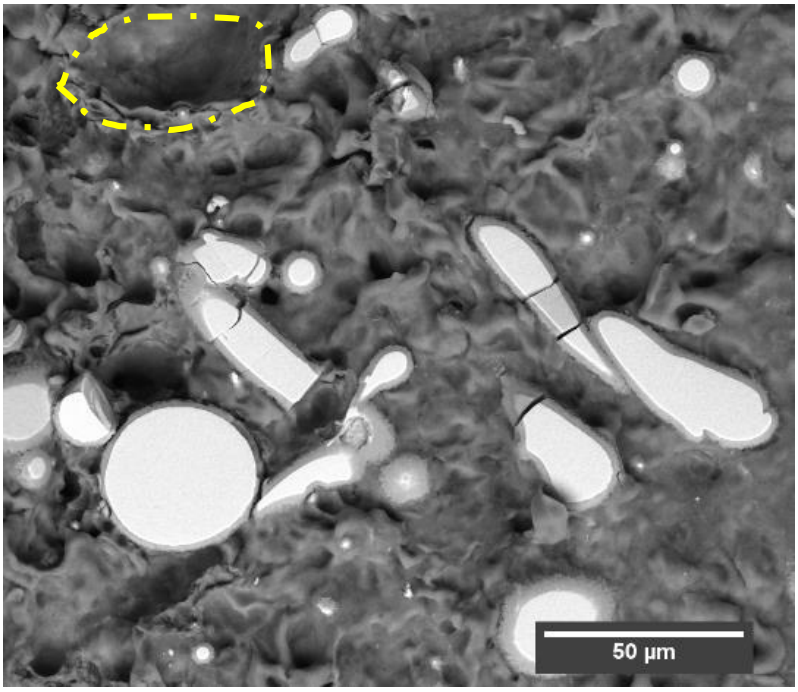

***Figure 4.17**: Back Scattered Electron image of Al-10 FMG composite. An ellipsoidal crater is seen on the top left of the image (highlighted with yellow dotted line) formed as a result of reinforcement loss*

Mostly the coarse particles are vulnerable to fracture. Larger the particle size, higher is the probability of containing inclusions and defects rendering them more susceptible to crack. A thin interfacial layer measuring 1– 3 µm in width surrounding the particles is visible in the BSE image. The nature of the interface plays a crucial role in determining the cavitation resistance of a composite. Here, aluminum surrounding the reinforcement particles have eroded. Particles are anchored into the matrix by the strong interfacial layer, which maintains bonding between the matrix and the reinforcement. Following the ductile tear of the matrix and brittle fracture of FMG, the interfacial layer is damaged, and the particle loses cohesion with the matrix and joins the debris. It should be noted that even when the particles are fractured, they remain embedded in the matrix and contribute to resisting the cavitation. However, their full potential cannot be utilized as they get debonded from the matrix early in undamaged or mildly damaged condition.

The schematic diagram in Fig. 4.18 gives a clear visualization of the erosion mechanism. The particle is assumed to be encapsulated by the matrix and the influence of another particle in the vicinity is ignored. The eruption of the vapor bubbles and the formation of micro-jets cause the crack initiation on the surface. The stress exerted initiates cracks, produces crater, and propagates it further upon longer exposure to the cavitation. When the crack lengthens enough to merge with another one, the material around it gets detached and joins the debris. In the later stage of cavitation, the interface gets eroded. Since the interface is a result of FMG and aluminum reaction, it is expected to have lower yield strength than the FMG and be stronger than aluminum. The BSE image in Fig. 4.18 shows an agreement with this claim where the interface is seen wearing off in a brittle manner after the surrounding matrix has eroded. Once the interfacial layer is lost, the particle gets detached, leaving a crater on the surface, as seen in Fig. 4.17. As discussed earlier, a higher volume fraction of the reinforcements leads to the network formation, resembling a fiber-like

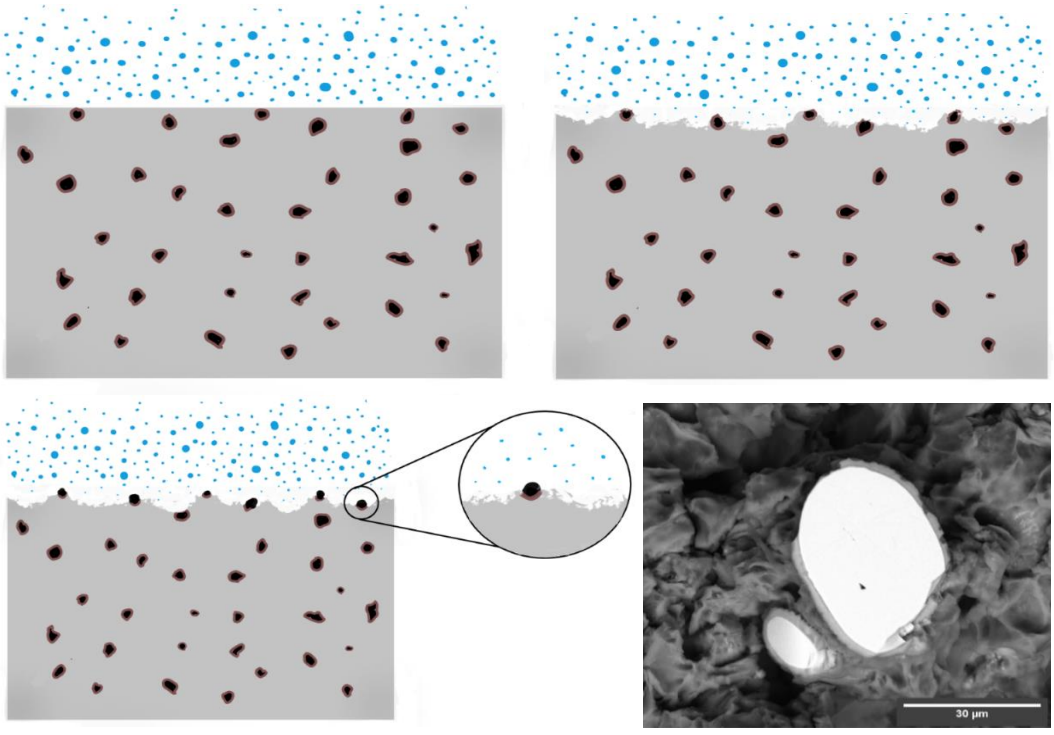

***Figure 4.18**: Cavitation erosion stages explained using the schematic. The corresponding BSE image highlights the interface erosion with surrounding matrix material eroded in Al-10 FMG*

arrangement. As a response to the cavitation, the reinforcements in the form of the network last longer. There is a possibility that once the interface is eroded, the entire chain would be detached, leading to a formation of larger crater. Despite that, the erosion resistance of Al-20 FMG and Al-30 FMG is superior to that of Al-10 FMG composite. The degree of particle contiguity influences the extent of distortion, and hence, Al- 40 FMG with the longest reinforcement network erodes least in the longer cavitation exposure.

Fig. 4.19 represents the elemental mapping of the eroded portion of Al-30 FMG after being exposed for 15 min cavitation. It appears that the aluminum adheres well to the surface of the FMG reinforcement particle. The diffused halo of aluminum on the particle boundary represents the interfacial diffusion layer.

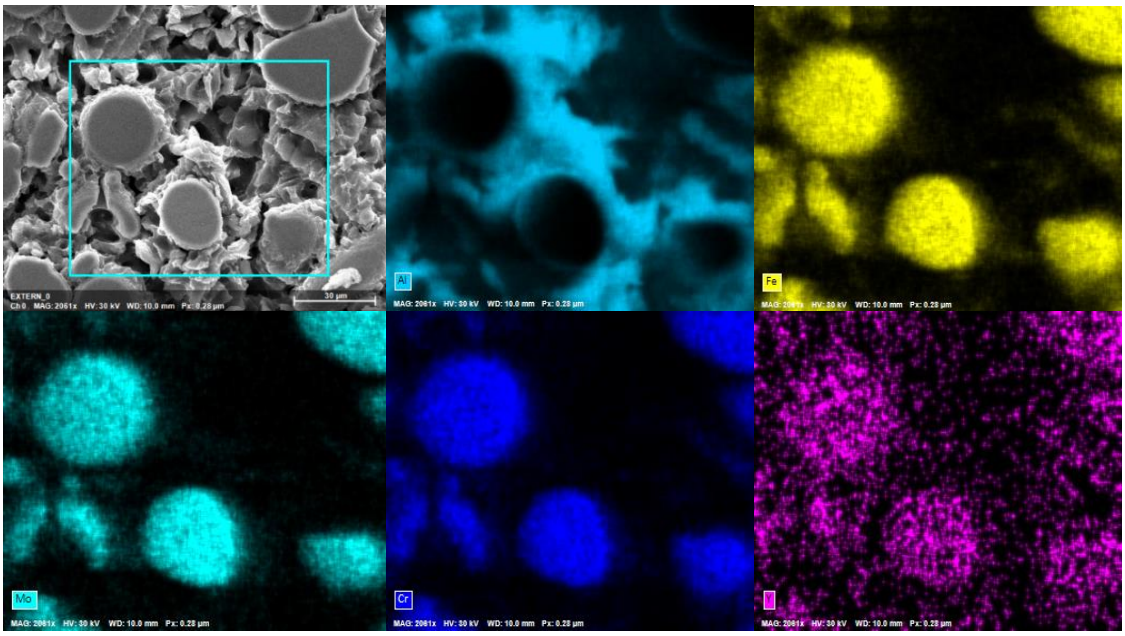

***Figure 4.19**: Elemental mapping of Al-30 FMG after being exposed to the cavitation*

CHAPTER V

CONCLUSIONS

5.1 Dry sliding wear behavior of the composite

Aluminum composites reinforced with $Fe_{48}Cr_{15}Mo_{14}Y_2C_{15}B_6$ metallic glass were successfully processed using the spark plasma sintering. The sintering was performed in the super-cooled liquid region of the metallic glass, and the viscous flow behavior is utilized to obtain the fully dense compacts. The non-linear increase in the hardness of the composite is explained using the shear lag model and particle contiguity. Room temperature sliding wear tests revealed that the addition of Fe-based glassy reinforcement is effective in improving the wear resistance of aluminum. The presence of a strong and uniform interlayer between the metallic glass particles and the matrix enables efficient load transfer between the two phases. With the reinforcement addition, the deformation mode shifts from ploughing to three-body abrasive material removal. An increase in the particle contiguity facilitates the formation of continuous reinforcement networks, and the plastic deformation of aluminum is suppressed. With the repeated movement of Si_3N_4 ball, the metallic glass particles fracture into submicron-sized fragments and eventually joins the debris. The wear mechanism is supported by SEM and EDS analysis. The findings of this study support the potential for the development of wear-resistant metallic glass reinforced aluminum matrix composites. The optimum content of the FMG reinforcement in aluminum for better tribological resistance is 40 vol.% where a sharp increase in the hardness of the composite is observed.

5.2 Cavitation erosion behavior of the composite

Cavitation erosion resistance of aluminum matrix composites increases with the FMG reinforcement addition from 10 vol.% to 40 vol.%. Short range atomic diffusion between aluminum and FMG reinforcement leads to the formation of a strong interfacial layer that resists the detachment FMG particle from the matrix during cavitation. Analysis of the eroded areas revealed the deformation mechanism. Average penetration depth decreases with the increase in reinforcement volume fraction. With increasing particle contiguity, the reinforcement networks create a dense barrier to suppress the distortion. As a result, Al-FMG composite exhibited a reduced average penetration depth in comparison with the pure Al compacts. The area occupied by the deeper penetration clusters such as 30 – 60 µm and 60 – 90 µm reduces from pure Al to Al-40 FMG. Analysis of the BSE micrograph supports the erosion mechanism proposed through the schematic. It was confirmed that once the interface erodes, the reinforcement particle gets detached without being used to its full potential. The cavitation erosion resistance depends primarily on surface conditions. Finer reinforcements occupying larger surface areas can resist the distortion more effectively. The effect of particle contiguity is prevalent in the cavitation erosion mechanism. These findings can help to investigate the methods further to improve the cavitation erosion resistance of the AMCs.

REFERENCES

[1] C. T. Lynch and J. P. Kershaw, *Metal matrix composites*. 2018.

[2] S. T. Mavhungu, E. T. Akinlabi, M. A. Onitiri, and F. M. Varachia, "Aluminum Matrix Composites for Industrial Use: Advances and Trends," *Procedia Manuf.*, 2017.

[3] K. M. Shorowordi, T. Laoui, A. S. M. A. Haseeb, J. P. Celis, and L. Froyen, "Microstructure and interface characteristics of B4C, SiC and Al2O3 reinforced Al matrix composites: A comparative study," *J. Mater. Process. Technol.*, 2003.

[4] J. Wang, Z. Li, G. Fan, H. Pan, Z. Chen, and D. Zhang, "Reinforcement with graphene nanosheets in aluminum matrix composites," *Scr. Mater.*, 2012.

[5] L. A. Yolshina, R. V. Muradymov, I. V. Korsun, G. A. Yakovlev, and S. V. Smirnov, "Novel aluminum-graphene and aluminum-graphite metallic composite materials: Synthesis and properties," *J. Alloys Compd.*, 2016.

[6] S. Gatea, H. Ou, and G. McCartney, "Deformation and fracture characteristics of Al6092/SiC/17.5p metal matrix composite sheets due to heat treatments," *Mater. Charact.*, 2018.

[7] S. Jayalakshmi, R. Singh, and M. Gupta, "Metallic Glasses as Potential Reinforcements in Al and Mg Matrices: A Review," *Technologies*, vol. 6, no. 2, p. 40, 2018.

[8] M. Aljerf, K. Georgarakis, D. Louzguine-Luzgin, A. Le Moulec, A. Inoue, and A. R. Yavari, "Strong and light metal matrix composites with metallic glass particulate reinforcement," *Mater. Sci. Eng. A*, vol. 532, pp. 325–330, 2012.

[9] S. Jayalakshmi and M. Gupta, *Metallic Amorphous Alloy Reinforcements in Light Metal Matrices*. 2015.

[10] F. A. Girot, J. M. Quenisset, and R. Naslain, "Discontinuously-reinforced aluminum matrix composites," *Compos. Sci. Technol.*, 1987.

[11] D. J. Lloyd, "Particle reinforced aluminium and magnesium matrix composites," *Int. Mater. Rev.*, 1994.

[12] A. Mazahery and M. O. Shabani, "Characterization of cast A356 alloy reinforced with nano SiC composites," *Trans. Nonferrous Met. Soc. China (English Ed.*, 2012.

[13] W. S. Miller and F. J. Humphreys, “Strengthening mechanisms in particulate metal matrix composites,” *Scr. Metall. Mater.*, 1991.

[14] A. G. Metcalfe and M. J. Klein, “Interfaces in fabricated metal matrix composites,” *J. Adhes.*, 1973.

[15] E. Hajjari, M. Divandari, and A. R. Mirhabibi, “The effect of applied pressure on fracture surface and tensile properties of nickel coated continuous carbon fiber reinforced aluminum composites fabricated by squeeze casting,” *Mater. Des.*, 2010.

[16] C. S. Ramesh, R. Keshavamurthy, B. H. Channabasappa, and A. Ahmed, “Microstructure and mechanical properties of Ni-P coated Si3N4 reinforced Al6061 composites,” *Mater. Sci. Eng. A*, 2009.

[17] C. A. León and R. A. L. Drew, “The influence of nickel coating on the wettability of aluminum on ceramics,” in *Composites Part A: Applied Science and Manufacturing*, 2002.

[18] I. B. Ozsoy, H. Choi, P. Joseph, G. Li, I. Luzinov, and H. Zhao, “Reinforced thermoplastic composites with interfacial microarchitectural anchoring: Computational study,” *Int. J. Solids Struct.*, vol. 112, pp. 54–64, 2017.

[19] M. F. Ashby, “The deformation of plastically non-homogeneous materials,” *Philos. Mag.*, 1970.

[20] Y. Li *et al.*, “Investigation of aluminum-based nanocomposites with ultra-high strength,” *Mater. Sci. Eng. A*, 2009.

[21] D. P. Myriounis, S. T. Hasan, and T. E. Matikas, “Microdeformation behaviour of Al-SiC metal matrix composites,” *Compos. Interfaces*, 2008.

[22] F. Bouafia, B. Serier, and B. A. B. Bouiadjra, “Finite element analysis of the thermal residual stresses of SiC particle reinforced aluminum composite,” *Comput. Mater. Sci.*, 2012.

[23] W. Klement, R. H. Willens, and P. Duwez, “Non-crystalline structure in solidified Gold-Silicon alloys,” *Nature*, 1960.

[24] C. Suryanarayana and A. Inoue, “Iron-based bulk metallic glasses,” *International Materials Reviews*. 2013.

[25] C. Suryanarayana, I. Seki, and A. Inoue, “A critical analysis of the glass-forming ability of alloys,” *J. Non. Cryst. Solids*, 2009.

[26] C. C. Hays, C. P. Kim, and W. L. Johnson, “Large supercooled liquid region and phase separation in the Zr-Ti-Ni-Cu-Be bulk metallic glasses,” *Appl. Phys. Lett.*, 1999.

[27] D. V. Dudina *et al.*, “Cu-based metallic glass particle additions to significantly improve overall compressive properties of an Al alloy,” *Compos. Part A Appl. Sci. Manuf.*, vol. 41, no. 10, pp. 1551–1557, 2010.

[28] B. Ashish Kumar Singh, S. P. Harimkar, and J. C. Hanan Raman P Singh Ranji Vaidyanathan, “DENSIFICATION BEHAVIOR, NANOCRYSTALLIZATION, AND MECHANICAL PROPERTIES OF SPARK PLASMA SINTERED Fe-BASED BULK

AMORPHOUS ALLOYS," 2010.

[29] J. Schroers, Q. Pham, and A. Desai, "Thermoplastic forming of bulk netallic glass - A technology for MEMS and microstructure fabrication," *J. Microelectromechanical Syst.*, 2007.

[30] R. Hasegawa, "Soft magnetic properties of metallic glasses," *J. Magn. Magn. Mater.*, 1984.

[31] J. Blink, J. Farmer, J. Choi, and C. Saw, "Applications in the nuclear industry for thermal spray amorphous metal and ceramic coatings," in *Metallurgical and Materials Transactions A: Physical Metallurgy and Materials Science*, 2009.

[32] M. H. Lee, J. H. Kim, J. S. Park, J. C. Kim, W. T. Kim, and D. H. Kim, "Fabrication of Ni-Nb-Ta metallic glass reinforced Al-based alloy matrix composites by infiltration casting process," *Scr. Mater.*, 2004.

[33] S. Jayalakshmi, S. Gupta, S. Sankaranarayanan, S. Sahu, and M. Gupta, "Structural and mechanical properties of Ni60Nb40 amorphous alloy particle reinforced Al-based composites produced by microwave-assisted rapid sintering," *Mater. Sci. Eng. A*, 2013.

[34] Z. Wang, M. S. Xie, W. W. Zhang, C. Yang, G. Q. Xie, and D. V. Louzguine-Luzgin, "Achieving super-high strength in an aluminum based composite by reinforcing metallic glassy flakes," *Mater. Lett.*, 2020.

[35] P. Gong, L. Deng, J. Jin, S. Wang, X. Wang, and K. Yao, "Review on the research and development of Ti-based bulk metallic glasses," *Metals*, vol. 6, no. 11. 2016.

[36] Z. Wang, M. Song, C. Sun, D. Xiao, and Y. He, "Effect of extrusion and particle volume fraction on the mechanical properties of SiC reinforced Al-Cu alloy composites," *Mater. Sci. Eng. A*, 2010.

[37] M. S. Xie, Z. Wang, G. Q. Zhang, C. Yang, W. W. Zhang, and K. G. Prashanth, "Microstructure and mechanical property of bimodal-size metallic glass particle-reinforced Al alloy matrix composites," *J. Alloys Compd.*, 2020.

[38] H. L. Rizkalla and A. Abdulwahed, "Some mechanical properties of metal-nonmetal Al-SiO2 particulate composites," *J. Mater. Process. Technol.*, 1996.

[39] S. Scudino *et al.*, "Mechanical properties of Al-based metal matrix composites reinforced with Zr-based glassy particles produced by powder metallurgy," *Acta Mater.*, vol. 57, no. 6, pp. 2029–2039, 2009.

[40] M. Tokita, E. Bldg, K. Sc, and P. Ksp, "Mechanism of Spark Plasma Sintering," *Ceramics*, 2011.

[41] A. P. Srivastava, M. Tong, T. Ștefanov, and D. J. Browne, "Elimination of porosity in bulk metallic glass castings using hot isostatic pressing," *J. Non. Cryst. Solids*, 2017.

[42] S. Scudino *et al.*, "Production and mechanical properties of metallic glass-reinforced Al-based metal matrix composites," in *Journal of Materials Science*, 2008.

[43] J. E. Garay, "Current-Activated, Pressure-Assisted Densification of Materials," *Annu. Rev. Mater. Res.*, 2010.

[44] D. M. Hulbert *et al.*, “The absence of plasma in ‘spark plasma sintering,’” *J. Appl. Phys.*, 2008.

[45] K. R. Anderson, J. R. Groza, M. Fendorf, and C. J. Echer, “Surface oxide debonding in field assisted powder sintering,” *Mater. Sci. Eng. A*, 1999.

[46] N. Saheb *et al.*, “Spark plasma sintering of metals and metal matrix nanocomposites: A review,” *Journal of Nanomaterials*. 2012.

[47] Z. Wang *et al.*, “Microstructure and mechanical behavior of metallic glass fiber-reinforced Al alloy matrix composites,” *Sci. Rep.*, vol. 6, no. April, pp. 1–11, 2016.

[48] G. Straffelini, “Wear mechanisms,” *Springer Tracts Mech. Eng.*, vol. 11, pp. 85–113, 2015.

[49] J. F. Archard, “Contact and rubbing of flat surfaces,” *J. Appl. Phys.*, 1953.

[50] B. Prakash and K. Hiratsuka, “Sliding wear behaviour of some Fe-, Co- and Ni-based metallic glasses during rubbing against bearing steel,” *Tribol. Lett.*, 2000.

[51] Y. Li, Y. Lian, and Y. Sun, “Cavitation erosion behavior of friction stir processed nickel aluminum bronze,” *J. Alloys Compd.*, 2019.

[52] M. S. Plesset and R. B. Chapman, “Collapse of an initially spherical vapour cavity in the neighbourhood of a solid boundary,” *J. Fluid Mech.*, 1971.

[53] S. Giorgini, *Lecture Notes on Statistical Mechanics - Course for the Master degree in Physics at the University of Trento from 2010 to 2015 (misprints amended and solution to problems added)*. 2016.

[54] B. Vyas and C. M. Preece, “Stress produced in a solid by cavitation,” *J. Appl. Phys.*, 1976.

[55] M. Duraiselvam, R. Galun, V. Wesling, B. L. Mordike, R. Reiter, and J. Oligmüller, “Cavitation erosion resistance of AISI 420 martensitic stainless steel laser-clad with nickel aluminide intermetallic composites and matrix composites with TiC reinforcement,” *Surf. Coatings Technol.*, 2006.

[56] H. S. Arora, H. S. Grewal, H. Singh, and S. Mukherjee, “Zirconium based bulk metallic glass-Better resistance to slurry erosion compared to hydroturbine steel,” *Wear*, 2013.

[57] W. J. Tomlinson and S. J. Matthews, “Cavitation erosion of aluminium alloy matrix/ceramic composites,” *J. Mater. Sci. Lett.*, 1994.

[58] K. Kondoh, J. Umeda, and R. Watanabe, “Cavitation resistance of powder metallurgy aluminum matrix composite with AlN dispersoids,” *Mater. Sci. Eng. A*, 2009.

[59] M. Ćosić, M. Dojčinović, and Z. Aćimović-Pavlović, “Fabrication and behaviour of Al–Si/SiC composite in cavitation conditions,” *Int. J. Cast Met. Res.*, vol. 27, no. 1, pp. 49–55, 2014.

[60] V. M. Maksimović, A. B. Devečerski, A. Došen, I. Bobić, M. D. Erić, and T. Volkov-Husović, “Comparative Study on Cavitation Erosion Resistance of A356 Alloy and A356FA5 Composite,” *Trans. Indian Inst. Met.*, vol. 70, no. 1, pp. 97–105, 2017.

[61] ASTM G32, “Standard Test Method for Cavitation Erosion Using Vibratory Apparatus,” *Annu. B. ASTM Stand.*, 2016.

[62] H. Y. Wang, Q. C. Jiang, Y. Wang, B. X. Ma, and F. Zhao, “Fabrication of TiB2 participate reinforced magnesium matrix composites by powder metallurgy,” *Mater. Lett.*, vol. 58, no. 27–28, pp. 3509–3513, 2004.

[63] A. Singh, S. R. Paital, A. Andapally, N. B. Dahotre, and S. P. Harimkar, “Densification behavior and wear response of spark plasma sintered iron-based bulk amorphous alloys,” *Adv. Eng. Mater.*, 2012.

[64] A. Singh, S. R. Bakshi, A. Agarwal, and S. P. Harimkar, “Microstructure and tribological behavior of spark plasma sintered iron-based amorphous coatings,” *Mater. Sci. Eng. A*, 2010.

[65] D. J. Wang, Y. J. Huang, J. Shen, Y. Q. Wu, H. Huang, and J. Zou, “Temperature influence on sintering with concurrent crystallization behavior in Ti-based metallic glassy powders,” *Mater. Sci. Eng. A*, 2010.

[66] N. Kang, Y. Fu, P. Coddet, B. Guelorget, H. Liao, and C. Coddet, “On the microstructure, hardness and wear behavior of Al-Fe-Cr quasicrystal reinforced Al matrix composite prepared by selective laser melting,” *Mater. Des.*, 2017.

[67] P. Zhang, S. X. Li, and Z. F. Zhang, “General relationship between strength and hardness,” *Mater. Sci. Eng. A*, vol. 529, no. 1, pp. 62–73, 2011.

[68] M. J. Starink and S. Syngellakis, “Shear lag models for discontinuous composites: Fibre end stresses and weak interface layers,” *Mater. Sci. Eng. A*, 1999.

[69] ASM International, *ASM Handbook Volume 2 Properties and Selection: Nonferrous Alloys and Special -Purpose Materials*. 2001.

[70] A. Miserez and A. Mortensen, “Fracture of aluminium reinforced with densely packed ceramic particles: Influence of matrix hardening,” *Acta Mater.*, 2004.

[71] A. Al-Hashem, A. Abdullah, and W. Riad, “The Effect of Alloy Microstructure on Their Cavitation Erosion Behavior in Seawater,” in *Cavitation - Selected Issues*, 2018.

VITA

SHUBHANKAR PADWAL

Candidate for the Degree of

Master of Science

Thesis: TRIBOLOGICAL AND CAVITATION EROSION BEHAVIOR OF METALLIC GLASS REINFORCED ALUMINUM MATRIX COMPOSITES PROCESSED USING SPARK PLASMA SINTERING

Major Field: Mechanical and Aerospace Engineering

Biographical:

Education:

Completed the requirements for the Master of Science in Mechanical and Aerospace Engineering at Oklahoma State University, Stillwater, Oklahoma in July, 2020.

Completed the requirements for the Bachelor of Technology in Metallurgical Engineering at College of Engineering, Pune, India in May, 2018.

Experience: Graduate research and teaching assistant in Mechanical and Aerospace Engineering department at Oklahoma State University.